BEILSTEIN JOURNAL OF NANOTECHNOLOGY

Chemical sensors based on quasi-one-dimensional nanostructured materials

Edited by Elisabetta Comini and Dario Zappa

Imprint

Beilstein Journal of Nanotechnology
www.bjnano.org
ISSN 2190-4286
Email: journals-support@beilstein-institut.de

The *Beilstein Journal of Nanotechnology* is published by the Beilstein-Institut zur Förderung der Chemischen Wissenschaften.

Beilstein-Institut zur Förderung der Chemischen Wissenschaften
Trakehner Straße 7–9
60487 Frankfurt am Main
Germany
www.beilstein-institut.de

BEILSTEIN JOURNAL OF NANOTECHNOLOGY

Features and advantages of flexible silicon nanowires for SERS applications

Hrvoje Gebavi[1,2], Vlatko Gašparić[1,2], Dubravko Risović[1,2], Nikola Baran[1,2], Paweł Henryk Albrycht[3] and Mile Ivanda[*1,2]

Full Research Paper

Open Access

Address:
[1]Ruđer Bošković Institute, Division of Materials Physics, Laboratory for Molecular Physics and Synthesis of New Materials, Bijenička cesta 54, Zagreb, Croatia, [2]Center of Excellence for Advanced Materials and Sensing Devices, Research Unit New Functional Materials, Bijenička cesta 54, Zagreb, Croatia and [3]Institute of Physical Chemistry, Polish Academy of Sciences, Kasprzaka 44/52, 01-224 Warsaw, Poland

Email:
Mile Ivanda* - ivanda@irb.hr

* Corresponding author

Keywords:
flexible hot spots; horizontal silicon nanowires; 4-mercaptophenylboronic acid; surface-enhanced Raman spectroscopy (SERS); vapour–liquid–solid

Beilstein J. Nanotechnol. **2019,** *10,* 725–734.
doi:10.3762/bjnano.10.72

Received: 10 January 2019
Accepted: 07 March 2019
Published: 15 March 2019

This article is part of the thematic issue "Chemical sensors based on quasi-one-dimensional nanostructured materials".

Guest Editor: D. Zappa

Abstract

The paper reports on the features and advantages of horizontally oriented flexible silicon nanowires (SiNWs) substrates for surface-enhanced Raman spectroscopy (SERS) applications. The novel SERS substrates are described in detail considering three main aspects. First, the key synthesis parameters for the flexible nanostructure SERS substrates were optimized. It is shown that fabrication temperature and metal-plating duration significantly influence the flexibility of the SiNWs and, consequently, determine the SERS enhancement. Second, it is demonstrated how the immersion in a liquid followed by drying results in the formation of SiNWs bundles influencing the surface morphology. The morphology changes were described by fractal dimension and lacunar analyses and correlated with the duration of Ag plating and SERS measurements. SERS examination showed the optimal intensity values for SiNWs thickness values of 60–100 nm. That is, when the flexibility of the self-assembly SiNWs allowed hot spots occurrence. Finally, the test with 4-mercaptophenylboronic acid showed excellent SERS performance of the flexible, horizontally oriented SiNWs in comparison with several other commercially available substrates.

Introduction

The mechanism of surface-enhanced Raman spectroscopy (SERS) [1] is predominantly described by electromagnetic theory, which covers most of the observed features [2]. Specially designed nanostructured surfaces, preferably with clusters of metal nanoparticles, sharp edges and tips, are the key to strong electromagnetic enhancement ranging from 10^{10} to

10^{14} [3]. If the values of Raman cross section of the analyte and of SERS enhancement are appropriate, even single-molecule detection is possible. For example, under resonant laser excitation of analyte molecules with differential cross section of ca. 10^{-27} cm^2/sr, a SERS enhancement factor (EF) of 10^8 would be adequate for single-molecule detection. Under non-resonant conditions and/or for lower cross sections (ca. 10^{-30} cm^2/sr) EF values above 10^{11} are required [4,5]. The possibility of detecting molecules at low concentrations leads to numerous applications in medicine [6], biology [7], gas [8] and chemical sensing [9], agriculture [10], food science [11,12]. Therefore, SERS is currently considered a hot topic in scientific research.

Generally, SERS-active nanostructures are used on either colloidal or solid substrates. A carefully prepared substrate for a specifically targeted molecule is of the crucial importance for the low SERS detection limit. The nanostructured surface significantly increases the effective SERS surface area of the substrates. Colloids are economical for synthesis, but suffer from the lack of reproducibility due to unpredictable aggregation. Thus, researchers have implemented various ways to control the aggregation, such as bifunctional linker molecules, stimuli-responsive polymers, short single-stranded DNA chains or aptamers. Optimized solid substrates offer high measurement reproducibility, stability, the possibility of precise spot-determined analyte detection and the measurement of water-insoluble substances [12].

Nowadays, the scientific focus is on a subcategory of solid substrates, i.e., “flexible SERS substrates”, which unlike the conventional solid substrates conform to the specific object and efficiently extract the target molecules [13-18]. They can withstand a tensile strain of up to 30% without losing the SERS features [13]. These flexible substrates include materials such as polydimethylsiloxane (PDMS) [13,15] or poly(methyl methacrylate) (PMMA) [14]. However, apart from the flexible substrates, also flexible nanostructures are reported on conventional, solid SERS substrates [19-21]. In these reports, vertically oriented silicon nanopillars in contact with a liquid would lean towards each other, trapping the targeted molecule. The Raman signal of these commercially available substrates exceeds that of competitors [19]. Therefore, these substrates can be considered as one of the top SERS substrates on the market.

We have synthesized similar flexible, but horizontally oriented silicon nanowires (SiNWs), and observed a significant increase of SERS intensity after immersion into the liquid. The surface tension of the liquid influences position and shape of the SiNWs. The SiNWs are displaced and pulled together in bundles. As a result, flexible hot spots with significantly increased SERS intensity occur. During the synthesis of flexible SiNWs the fabrication parameters are of a crucial importance. The small-diameter SiNWs synthesized and described in this paper are sensitive not only to the surface tension of the liquid. Their flexibility also depends on the metal plating [22]. The paper compares Ag-plated horizontally synthesized SiNWs with commercially available vertically aligned SiNWs for SERS applications utilizing 4-mercaptophenylboronic acid (4-MPBA) as a test molecule. To the best of our knowledge, flexible horizontally oriented SiNWs and the benefits of flexible hot spots for SERS have not been reported before.

We have compared the synthesized substrates (RBI) with commercially available substrates from Silmeco (https://www.silmeco.com), AtoID (http://atoid.com) and Sersitive (http://sersitive.eu). One should be aware that the presented results are obtained on only with a few commercially available substrates and that our intention is not to rate or evaluate, but rather the presentation of the first results.

Experimental

Horizontal silicon nanowires were fabricated by vapor–liquid–solid (VLS) synthesis in a low-pressure chemical vapor deposition (LPCVD) reactor as described in [23]. In short, Si wafers (<100> orientation, 5–10 Ω·cm resistivity, p-type) were cleaned following the standard RCA (Radio Corporation of America) cleaning processes [24], followed by Au sputtering in a Polaron E5000 sputter coater at ca. $5{\cdot}10^{-4}$ mbar work pressure. Prior to VLS synthesis, annealing in vacuum for one hour at temperatures from 480–560 °C was performed. In the VLS process, 26% SiH_4 diluted in Ar with 270 sccm flow rate was deposited for 1 h. In each experiment, the annealing temperature was the same as the VLS process temperature. The Ag nanoparticle decoration of the horizontal SiNWs obtained in the previous step was obtained by the same sputtering system after different time durations (3, 5, 7, 16, 20 and 30 min). Afterwards, the ca. 3 × 3 mm^2 squared samples were immersed in an ethanol solution of 4-mercaptophenylboronic acid (4-MPBA) for several hours.

The morphology of the synthesized samples was monitored with a Jeol JSM 7000F scanning electron microscope under 10 kV discharge.

Raman spectroscopy measurements were performed using a Jobin Yvon T64000 Raman spectrometer in micro-single configuration. The laser power at 532 nm on the sample in the ca. 1 μm spot was 1–2 mW. For all experiments, a long-working-distance 50×/0.75 objective was used. The exposition time was 10 or 20 s per scan.

For the determination of fractal dimension and lacunarity, we used the ImageJ software [25] with the FracLac plugin. The data were extracted from grey-scale images using 'Box Counting – 'Differential volume Plus1' for grey-scale image analyses with "black background" as fixed option. The program operates with the equation: $D = 3 - (s/2)$, where s is the regression-line slope, and for the average fractal dimension,

$$\bar{D} = \sum_{G=1}^{\text{grids}} \frac{D(G)}{G},$$

where the summation is over all grids.

Results and Discussion

Dependence of SERS intensity on the VLS process temperature

The first step in the synthesis optimization of the horizontally oriented SiNW substrates includes the determination of the optimal VLS synthesis temperature. The color of the substrates ranged from pale yellow to dark brown (Supporting Information File 1, Figure S1). The color change clearly indicates changes of thickness and morphology of the SiNWs induced by the processing temperature (Supporting Information File 1, Figure S2). Roughly, the SiNW diameter increases with VLS process temperature from 50 to 150 nm. Similar values and a linear correlation between temperature and thickness were reported in [26].

4-MPBA was chosen as a SERS test molecule because of the strong affinity between the thiol group and metal surfaces (Ag or Au) as well as because of the easy formation of self-assembled monolayers (SAMs) [27]. Furthermore, the benzene ring is orientation-sensitive and has a relatively large Raman cross section (ca. 10^{-29} cm^2/sr [28]). The boronic acid group binds to certain analytes, for example, peptidoglycans in bacterial cell walls [29]. Recently, the difficult detection of saccharides (glucose, fructose) due to a low Raman scattering cross-section and a weak metal affinity was facilitated through the surface immobilization via 4-MPBA [30,31]. The 4-MPBA reporter features are predominantly based on re-orientation i.e. binding of the analyte via the boronic acid group causing a symmetry breaking and activation of the charge transfer mechanism which finally impacts SERS intensity [32].

It is also known that MPBA is pH-sensitive [30,33]. The bands at 1000 and 1073 cm^{-1} gradually decrease with increasimg pH value, which can be ascribed to the change of the angle between the S–H bond and the metal surface (Supporting Information File 1, Figure S3). With the increase of the pH value, the sp^2-hybridized boronic acid changes to the sp^3-hybridized boronate [33].

The fabricated horizontal SiNWs synthesized at different temperatures in the range from 480 to 560 °C were all sputtered with Ag for 5 min. After that, the samples were dipped in 10^{-4} M MPBA solution in ethanol for several hours in order to allow for the formation of SAMs. After the incubation, the samples were washed with milliQ water and dried for 1 h. SERS spectra are presented in Figure 1. The full-range 4-MPBA SERS spectrum is shown in Supporting Information File 1, Figure S4. The band assignments are given in Table S1 of Supporting Information File 1.

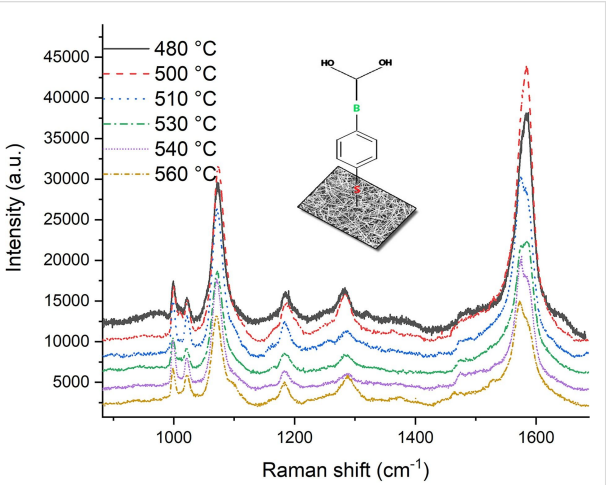

Figure 1: SERS spectra of 10^{-4} M 4-MPBA (inset) after immersion in H_2O for different VLS process temperatures.

Figure 2 shows the SERS intensities of the 1073 and 1574 cm^{-1} bands before and after H_2O washing for different VLS process temperatures. The optimal SERS signal is obtained for a temperature of 500 °C during the VLS process, and the SERS signal significantly increases after washing with water.

The first observation can be clearly explained as follows: The temperature during annealing prior to VLS synthesis influences the size and distribution of the Au seeds on the Si wafer, while the VLS process temperature determines growth rate and thickness of the SiNWs [34]. Geometry, density and the changes in surface morphology of the SiNWs influence the variations in SERS intensity.

The second observation can be explained in two ways. Firstly, 4-MPBA interacts with water; and secondly, EtOH or H_2O capillary forces influence the surface morphology of the substrate. The pH value of 100% ethanol is 7.33, while the water has a pH value equal to 7. Therefore, we do not expect a significant increase in SERS intensity due to the reorientation of 4-MPBA that could be ascribed to a small change of pH value (see the charge transfer and absorbance in [35]). The influence

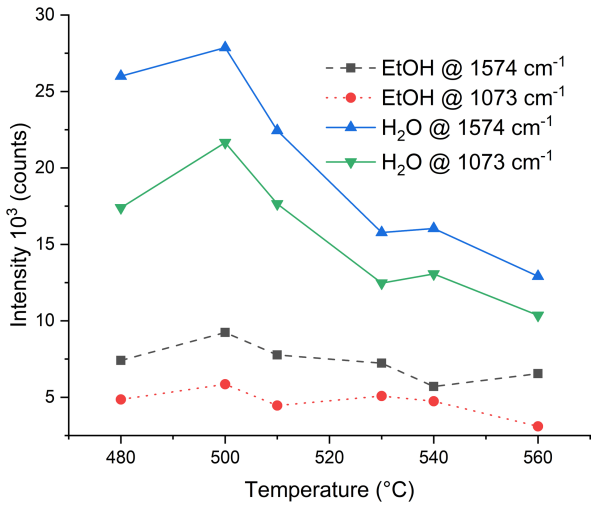

Figure 2: SERS intensities of the 1073 and 1574 cm^{-1} bands before (denoted EtOH) and after H_2O washing for different VLS process temperatures.

of the capillary forces will be discussed in the following sections.

Ag decoration and morphology of Si nanowires and immersion-induced changes

Using 500 °C as the optimal VLS process temperature, we decorated SiNWs through Ag sputtering. The sputtering time varied from 3 to 30 min. The corresponding SEM images recorded at a magnification of 100000× are shown in Figure 3.

The thickness of the SiNWs was measured at several points for each sputtering time and the average values are given in Figure S5 in Supporting Information File 1. It is shown that the thickness linearly increases with the sputtering time and these average values are used equivalently to the sputtering times in the remainder of the paper. The non-sputtered SiNWs have an average thickness of around 60 nm. In Figure 10 of [26], the authors reported approximately the same thickness of 60 nm after 1 h of VLS deposition at 500 °C.

After short sputtering times (3 and 5 min), the SiNWs are decorated with irregularly shaped droplets of 20–60 nm diameter (Supporting Information File 1, Figure S6). In the range from 7 to 10 min (Figure 3), the upper SiNW layer is completely covered with Ag, yielding Ag cylinders for SERS while in the lower SiNW layers there are only Ag nanoparticles. The lower SiNW layers contribute less to SERS amplification than the upper layer. Sputtering for 16 to 30 min completely covered the SiNWs with Ag, while the thickness increased with the sputtering time. The samples shown in Figure 3 were immersed in an ethanol solution of 4-MPBA and were subsequently washed in water. The complete set of SEM images is presented in Supporting Information File 1, Figures S7–S9, while selected images are given in Figure 4.

The first row in Figure 4 shows SiNWs sputtered with Ag for a time of 3 min. The first image shows the dry sample while the second and the third image show the same sample after immersion in ethanol and water. From these Figures, it can be concluded that the liquid immersion strongly influences the surface morphology of the SiNWs. Figure S10 in Supporting Information File 1 corroborates this observation. Ethanol and especially water pull the SiNWs together creating irregularly shaped bundles (Figure 5). To support this important observation the

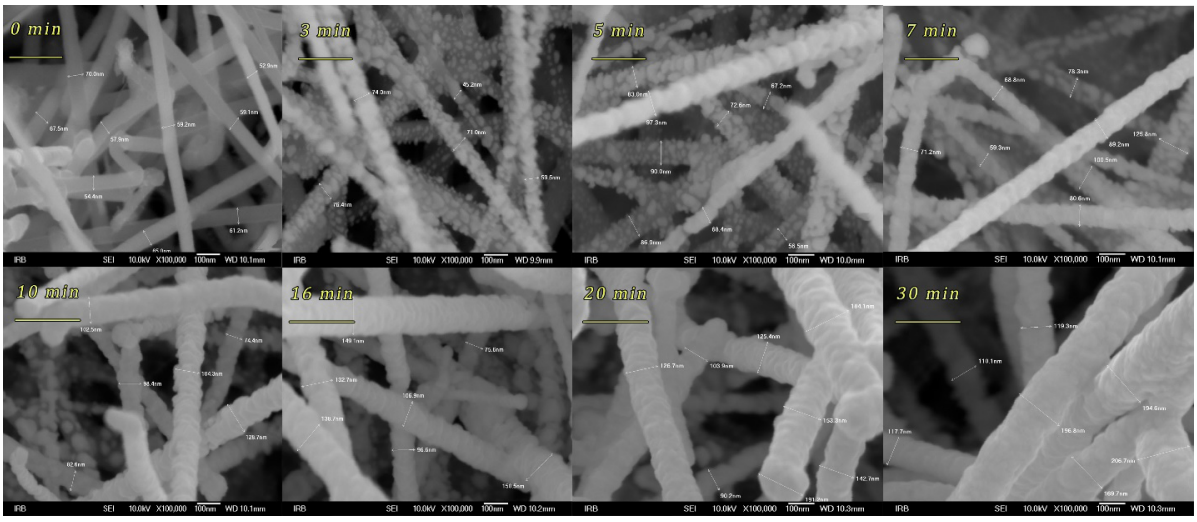

Figure 3: SEM images of horizontally in-plane randomly oriented SiNWs after different Ag sputtering times.

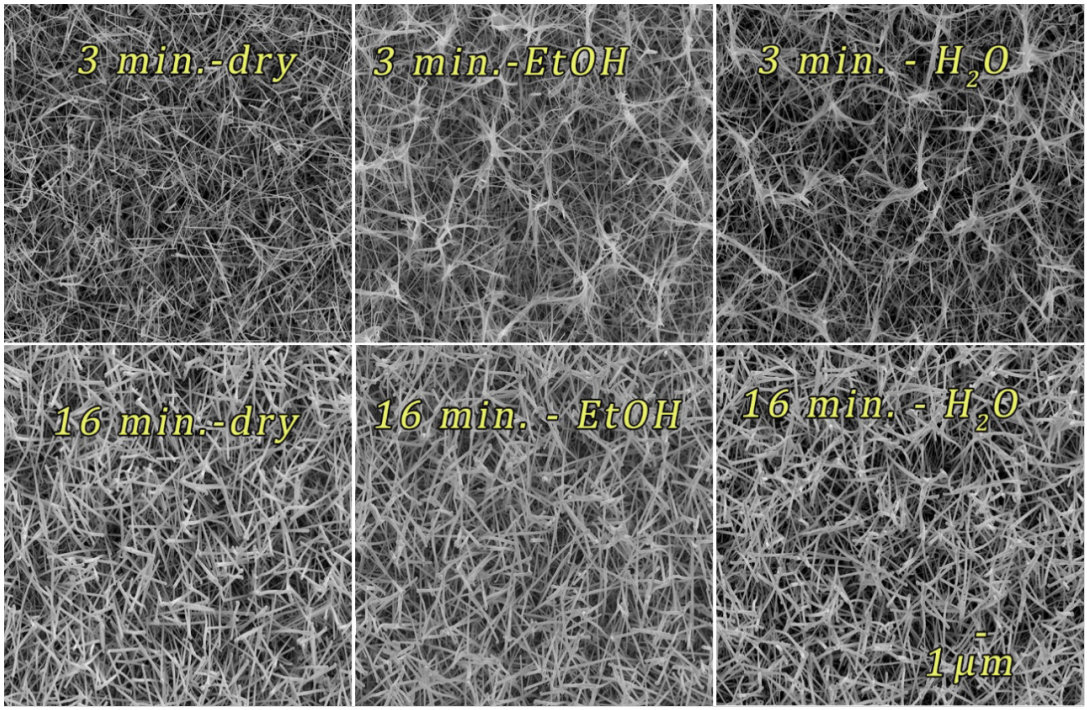

Figure 4: SEM images of dry samples in comparison with the one after immersion in EtOH and water for two different sputtering times of 3 and 16 min.

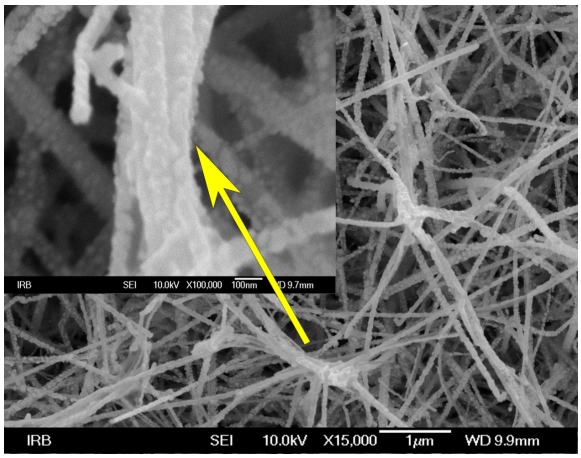

Figure 5: SEM images of SiNWs obtained through VLS deposition at 500 °C, then sputtered Ag for 3 min and finally immersed in H_2O.

SiNWs bundles are shown for different sputtering times in Supporting Information File 1, Figure S11. Furthermore, a shorter deposition time allows the SiNWs to move much easier than longer sputtering times (more than 16 min). From the comparison of the samples sputtered for 16 min, no significant change can be observed regardless the liquid immersion. Therefore, a sputtering time longer than 16 min (Supporting Information File 1, Figures S7–S9 and Figure S11) fixates the SiNWs, not allowing them to form bundles.

Flexibility of the vertical SiNWs can be achieved by a certain aspect ratio of SiNWs. In [36] the leaning of ca. 32 µm long and 80–200 nm thick SiNWs was observed prior to measurements. Flexible SiNWs with a different aspect ratio of 1:10, (100 nm in diameter and 1.0–1.3 µm in height) were reported in [37]. "Leaning fingertips" features were claimed in commercially available substrates [20] where the aspect ratio was ca. 1:15 with significantly shorter and thinner SiNWs (600 nm height and 40 nm thickness). Drawing the parallel between the horizontal and vertical SiNWs, we have also observed that the SiNW thickness influences the flexibility, i.e., the ability of SiNWs to bundle together. An even more important factor was Ag plating, which freezes the SiNWs contact points not allowing them to move. The length of horizontal SiNWs does not play a crucial role regarding the flexibility, but it is very important in order to give a high SiNWs surface density, which consequently guarantees uniform SERS signals at different locations of the substrate.

A closer look (Supporting Information File 1, Figure S10) shows that water has a stronger impact than ethanol on the surface morphology. This can be explained by the higher average number of hydrogen bonds in water (ca. 3.8) than in ethanol (ca. 2) and the, consequently, stronger surface tension, 72.86 and 22.39 $mN{\cdot}m^{-1}$ at 20 °C, respectively [38,39]. SiNWs are captured by the water surface tension through adhesive forces

[40] and during drying, the strong surface tension moves the SiNWs towards each other creating twisted and irregular SiNWs bundles. For the long sputtering times (when the SiNWs are completely covered with Ag), adhesion and surface tension are not strong enough to overcome the stiffening caused by sputtering.

Another significant substrate feature is surface wetting. Unlike vertical SiNWs [38], horizontal SiNWs are hydrophilic, as freshly prepared SiNW substrate as well as after Ag sputtering (Supporting Information File 1, Figure S12). The reasons are predominantly the characteristic surface roughness and the chemical affinity. Generally, the hydrophilic substrate surface is desirable for hydrophilic molecules such as for example dextrose and albumin [41].

SERS sensing of 4-MPBA

In order to determine the optimal Ag-sputtering time, we measured SERS spectra for four different 4-MPBA concentrations (10^{-3}, 10^{-4}, 10^{-5} and 10^{-6} M) at 100 different points. The mapping points, separated by 10 µm, were spaced in a 100 × 100 µm grid. Also, all samples were measured before and after immersion in H_2O.

The average SERS values of 4-MPBA ethanol solutions at different SiNWs thicknesses are shown in Supporting Information File 1, Figure S13. Figure 6 shows the average SERS values only after immersion in H_2O. The standard deviation was significantly higher for the lower (10^{-6} M) than for the higher (10^{-5} to 10^{-3} M) concentrations of 4-MPBA (Supporting Information File 1, Figure S14). The sample homogeneity is also shown by a colored-pixel map (Supporting Information File 1, Figure S14).

The SERS intensity not only depends on the SiNW thickness (sputtering time), but also on the 4-MPBA concentration. Adding more analyte will not increase the SERS intensity as much as it did between 10^{-6} and 10^{-5} M. It indicates that there is only a certain number of possible active sites on Ag that can host the analyte molecules. The reorientation of 4-MPBA or a shielding of the first analyte monolayer could also contribute to this effect.

At a concentration of 10^{-6} M, the best SERS results are achieved for thin SiNWs, while for higher concentrations the SERS intensity is quite constant up to ca. 120 nm thickness, after which it starts decreasing. The intensity decrease with increasing thickness shows that not only metal nanoparticle size and SiNW thickness are important for SERS enhancement, but also the quality of the hot spots. We can see that when Ag sputtering freezes the SiNW structure, SiNWs cannot aggregate to

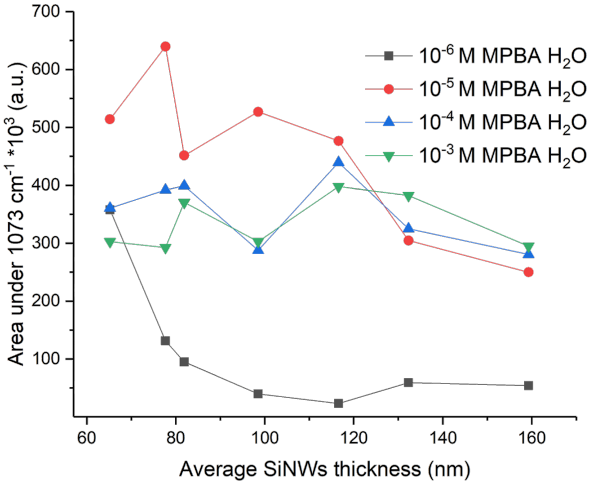

Figure 6: Average SERS values of 4-MPBA for different SiNW thicknesses after H_2O immersion.

bundles and consequently the SERS intensity decreases. A possible shift of the localized surface plasmon absorption band is out of the scope of this paper.

We can see a significant increase of the SERS signal at 10^{-5} M after water immersion (Figure 7). The same behavior is observed for other concentrations, however, sometimes the difference between the SERS intensities before and after water immersion is small (Supporting Information File 1, Figure S16). As reported in [42] we assume that capillary forces dominate over van der Waals forces by several orders of magnitude. During drying, the adhesion between liquid and SiNW surface pulls and bends the SiNWs, changing the substrate morphology and consequently increasing the SERS intensity. Water has a higher surface tension than ethanol and, consequently, pulls the

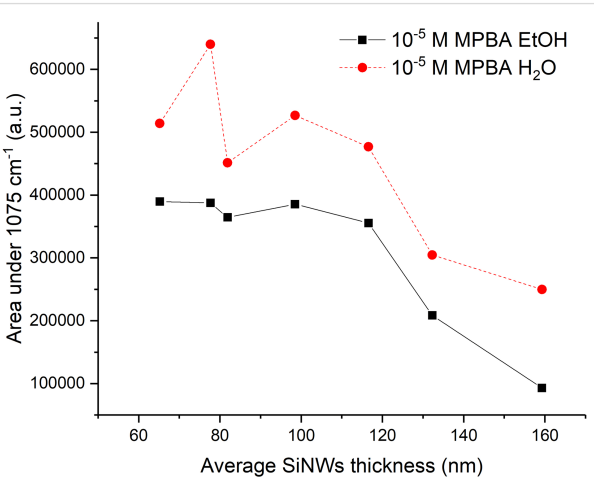

Figure 7: SERS enhancement after immersion in water.

SiNWs together stronger causing a larger SERS enhancement. Since the SERS effect decreases with distance [43], bringing the SiNWs closer significantly improves the analyte detection. In [2] the author assumed that the enhancement factor increases approximately as d^{-8} in the case of two metal nanoparticles with the polarization along the particle axis, which can be roughly applied to the case of two nanowires. However, in the reported substrates SiNWs are randomly oriented and the polarization measurement was not tested in detail.

Fractal dimension and lacunarity of Ag-plated SiNWs

Fractal dimension

In order to describe horizontal SiNW morphology in more detail, we calculated the average fractal dimension (D) from the SEM images (Supporting Information File 1, Figures S7–S9) for all SERS-active samples (Figure 8). FracLac delivers a measure of the box-counting fractal dimension, which is the measure of complexity, i.e., the change in detail with a change in scale. The average value of D is the usual box-counting fractal dimension averaged over the number of scans that carried out done at different grid positions [25]. For three-dimensional objects, the expected D values are between 2 and 3.

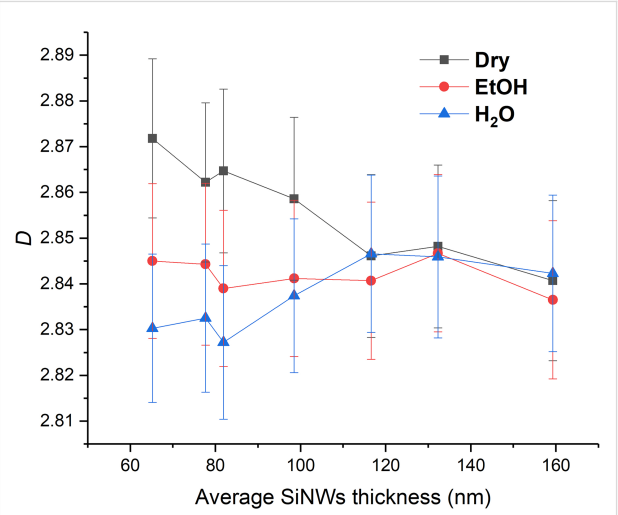

Figure 8: Fractal dimension (D) of Ag-plated SiNWs after immersion in EtOH and H_2O.

Figure 8 clearly shows that the fractal dimension decreases after the EtOH and H_2O immersion ($D_{dry} > D_{EtOH} > D_{water}$) for samples with an average SiNWs thickness below 120 nm. For average SiNWs thickness values of 120–160 nm, there is no change of the fractal dimension. Correlating these results with the SEM images (Supporting Information File 1, Figures S7–S9), one can see that Ag sputtering freezes the SiNWs structure and the fractal dimension remains constant. The second conclusion is that as the water pulls the SiNWs together (Supporting Information, File 1, Figure S10), the fractal dimension decreases (Figure 8). This leads to the creation of hot spots along the SiNWs which result in an enhanced SERS effect (Figure 7). After immersion in a liquid, there is not only a SiNW redistribution in the xy-plane, but also along the z-axis. However, this aspect is beyond the scope of this paper.

Lacunarity

Complementary to fractal dimension, lacunarity gives additional morphological information. As the cross junctions between AgNPs and SiNWs are important for the creation of hot spots and SERS enhancement, the nanosized gaps between SiNWs can behave as a resonant cave where the incident laser light is scattered numerous times further contributing to SERS amplification. Those voids can be described by lacunarity, which is considered a measure of heterogeneity (inhomogeneity) or translational or rotational invariance in an image [25]. Lacunarity values at the excitation wavelength of 532 nm are calculated as described in Supporting Information File 1 and shown in Figure 9.

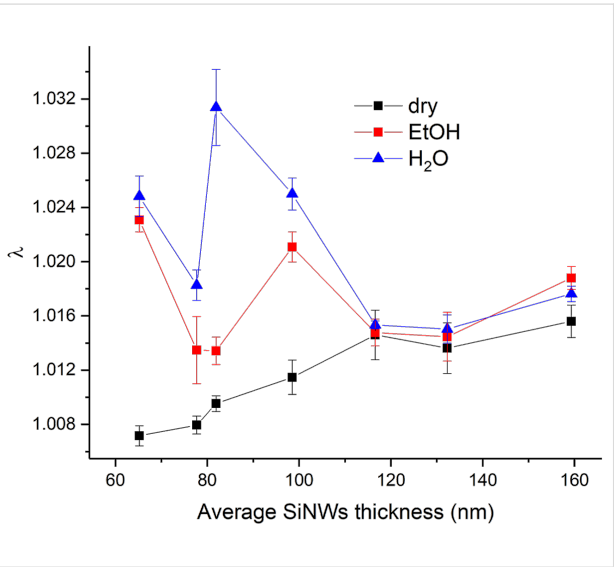

Figure 9: Lacunarity at 532 nm for different SiNWs thicknesses.

The lacunarity of dry substrates increases after immersion in EtOH and water. The lacunarity confirms the assumption drawn from the SEM images that the long sputtering time freezes the SiNW structure, making it impervious to immersion in liquid. Similar lacunar values for the three thickest samples are observed (Figure 9), analogous to the calculations of fractal dimension (Figure 8). Furthermore, the fractal dimension decreases after the immersions for thinner samples while the lacunarity increases. The decrease of the fractal dimension is the consequence of the SiNWs flexibility and their tendency to

bundle together. Consequently, it leaves bigger gaps that do not have the same width of the size distribution as in the case of dry samples. There are wider and different gap sizes resulting in the lacunarity increase. The analysis of fractal dimension and lacunarity shows the results after water immersion are more separated from the dry sample than the results after ethanol immersion, indicating that water places the SiNWs closer together than EtOH. The smaller the gaps between the SiNWs result in a stronger SERS effect.

Comparison with commercially available SERS substrates

The synthesized samples were compared with commercially available samples utilizing 10^{-5} M 4-MPBA solution in ethanol as analyte. SERS measurements were carried out on the same samples two times. The first one immediately after drying of EtOH (Supporting Information File 1, Figure S18) and the second one after immersion in milli-Q water and subsequent drying (Figure 10). The first SERS measurement showed similar values for all three commercially fabricated samples with somewhat lower values of our RBI lab sample.

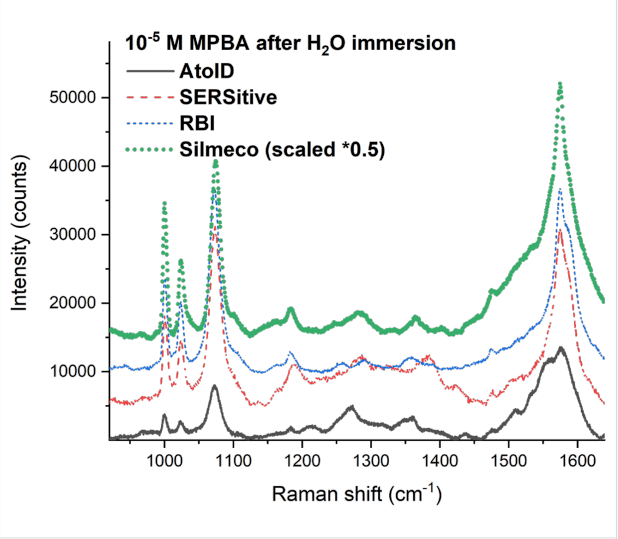

Figure 10: Comparison of the commercial SERS substrates and the synthetized sample (RBI) after the immersion in water.

After immersion in water, the SERS intensity was drastically different. Of all three samples used for the comparison only Silmeco has flexible SiNWs. Their SERS values showed a 2–3-times stronger intensity in comparison to the RBI spectrum recorded under the same conditions. Our lab sample showed a significant increase after immersion in water as well and becomes more than comparable with AtoID and SERSitive substrate spectra. A more detailed comparison between Silmeco and our lab samples is given in Supporting Information File 1, Figure S19.

These results show the advantage of the flexible nanostructures and self-assembled hot spots for SERS applications. We note here that the comparison of the commercially available SERS substrates is obtained on a reduced number of samples without detailed mapping and therefore is not a subject of the SERS market rating (Figure 11).

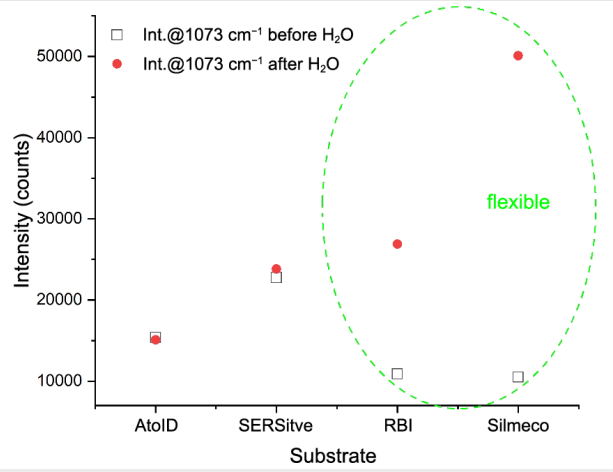

Figure 11: Intensity at 1073 cm^{-1} for the samples fabricated in different labs.

Conclusion

This research showed the advantages of SERS substrates with flexible silicon nanowires over solid substrates with a fixed structure. The fabrication process and impact of each preparation stage are presented in detail. It is shown that the optimal SiNWs thickness decorated with Ag is in the range from 60 to 100 nm. This thickness allows for the flexibility of the several micrometers long, horizontally placed and randomly oriented SiNWs. The strong SERS enhancement mechanism relies on bringing the SiNWs to nanogap-vicinity, which creates a system comparable to optical tweezers and allows for localized surface plasmons and strong electric fields to occur. The morphological surface changes after immersion in ethanol in water are described by analyzing scanning electron images, particularly by using fractal and lacunar analysis. The corresponding fractal dimensions and lacunarity at excitation wavelength are both not only compliant with each other, but also with SERS measurements. This result strongly encourages researchers to describe the solid substrates with fractal and lacunar information since they could correlate morphology and SERS measurements results. To the best of our knowledge, we have not seen detailed reports on SERS substrates with horizontally placed flexible silicon nanowires. The comparison with commercially available substrates utilizing 4-MPBA as a test molecule showed that these samples keep pace with the best SERS market products. These preliminary results are promising and encourage for further improvements.

Supporting Information

Supporting Information File 1

Additional experimental data.
[https://www.beilstein-journals.org/bjnano/content/supplementary/2190-4286-10-72-S1.pdf]

Acknowledgements

This work has been partially supported by SAFU, project 263 KK.01.1.1.01.0001., Croatian Science Foundation under the project (IP-2014-09-7046) and COST action BM1401 - Raman-based applications for clinical diagnostics (Raman4Clinics). The authors would like to thank Silmeco, SERSitive and AtoID companies for SERS substrates providing.

ORCID® iDs

Hrvoje Gebavi - https://orcid.org/0000-0002-0982-1417
Paweł Henryk Albrycht - https://orcid.org/0000-0002-2656-6892

References

1. Fleischmann, M.; Hendra, P. J.; McQuillan, A. J. *Chem. Phys. Lett.* **1974,** *26,* 163–166. doi:10.1016/0009-2614(74)85388-1
2. Moskovits, M. *J. Raman Spectrosc.* **2005,** *36,* 485–496. doi:10.1002/jrs.1362
3. Sujith, A.; Itoh, T.; Abe, H.; Yoshida, K.-i.; Kiran, M. S.; Biju, V.; Ishikawa, M. *Anal. Bioanal. Chem.* **2009,** *394,* 1803–1809. doi:10.1007/s00216-009-2883-9
4. Blackie, E. J.; Le Ru, E. C.; Etchegoin, P. G. *J. Am. Chem. Soc.* **2009,** *131,* 14466–14472. doi:10.1021/ja905319w
5. Zrimsek, A. B.; Wong, N. L.; Van Duyne, R. P. *J. Phys. Chem. C* **2016,** *120,* 5133–5142. doi:10.1021/acs.jpcc.6b00606
6. Lane, L. A.; Qian, X.; Nie, S. *Chem. Rev.* **2015,** *115,* 10489–10529. doi:10.1021/acs.chemrev.5b00265
7. Wang, Y.; Irudayaraj, J. *Philos. Trans. R. Soc., B* **2013,** *368,* 20120026. doi:10.1098/rstb.2012.0026
8. Rae, S. I.; Khan, I. *Analyst* **2010,** *135,* 1365. doi:10.1039/b924537e
9. Schlücker, S. *Angew. Chem., Int. Ed.* **2014,** *53,* 4756–4795. doi:10.1002/anie.201205748
10. Pang, S.; Yang, T.; He, L. *TrAC, Trends Anal. Chem.* **2016,** *85,* 73–82. doi:10.1016/j.trac.2016.06.017
11. Janči, T.; Mikac, L.; Ivanda, M.; Marušić Radovčić, N.; Medić, H.; Vidaček, S. *J. Raman Spectrosc.* **2017,** *48,* 64–72. doi:10.1002/jrs.4991
12. Xie, X.; Pu, H.; Sun, D.-W. *Crit. Rev. Food Sci. Nutr.* **2018,** *58,* 2800–2813. doi:10.1080/10408398.2017.1341866
13. Kumar, S.; Goel, P.; Singh, J. P. *Sens. Actuators, B* **2017,** *241,* 577–583. doi:10.1016/j.snb.2016.10.106
14. Xiu, X.; Guo, Y.; Li, C.; Li, Z.; Li, D.; Zang, C.; Jiang, S.; Liu, A.; Man, B.; Zhang, C. *Opt. Mater. Express* **2018,** *8,* 844–857. doi:10.1364/ome.8.000844
15. Park, S.; Lee, J.; Ko, H. *ACS Appl. Mater. Interfaces* **2017,** *9,* 44088–44095. doi:10.1021/acsami.7b14022
16. Yang, L.; Hu, J.; Bai, K. *J. Adhes. Sci. Technol.* **2016,** *30,* 566–578. doi:10.1080/01694243.2015.1111834
17. Wang, G.; Yi, R.; Zhai, X.; Bian, R.; Gao, Y.; Cai, D.; Liu, J.; Huang, X.; Lu, G.; Li, H.; Huang, W. *Nanoscale* **2018,** *10,* 16895–16901. doi:10.1039/c8nr04971h
18. Lu, G.; Lia, H.; Zhang, H. *Chem. Commun.* **2011,** *47,* 8560–8562. doi:10.1039/c1cc12027a
19. Schmidt, M. S.; Hübner, J.; Boisen, A. *Adv. Mater. (Weinheim, Ger.)* **2012,** *24,* OP11–OP18. doi:10.1002/adma.201103496
20. Wu, K.; Rindzevicius, T.; Schmidt, M. S.; Mogensen, K. B.; Xiao, S.; Boisen, A. *Opt. Express* **2015,** *23,* 12965. doi:10.1364/oe.23.012965
21. Wong, C. L.; Dinish, U. S.; Schmidt, M. S.; Olivo, M. *Anal. Chim. Acta* **2014,** *844,* 54–60. doi:10.1016/j.aca.2014.06.043
22. Galopin, E.; Barbillat, J.; Coffinier, Y.; Szunerits, S.; Patriarche, G.; Boukherroub, R. *ACS Appl. Mater. Interfaces* **2009,** *1,* 1396–1403. doi:10.1021/am900087s
23. Gebavi, H.; Ristić, D.; Baran, N.; Mikac, L.; Mohaček-Grošev, V.; Gotić, M.; Šikić, M.; Ivanda, M. *Mater. Res. Express* **2018,** *5,* 015015. doi:10.1088/2053-1591/aaa152
24. Kern, W. *J. Electrochem. Soc.* **1990,** *137,* 1887–1892. doi:10.1149/1.2086825
25. ImageJ. https://imagej.nih.gov/ij (accessed Dec 15, 2018).
26. Gadea, G.; Morata, A.; Santos, J. D.; Dávila, D.; Calaza, C.; Salleras, M.; Fonseca, L.; Tarancón, A. *Nanotechnology* **2015,** *26,* 195302. doi:10.1088/0957-4484/26/19/195302
27. Mosier-Boss, P. *Nanomaterials* **2017,** *7,* 142. doi:10.3390/nano7060142
28. Schomacker, K. T.; Delaney, J. K.; Champion, P. M. *J. Chem. Phys.* **1986,** *85,* 4240–4247. doi:10.1063/1.451795
29. Wang, P.; Pang, S.; Pearson, B.; Chujo, Y.; McLandsborough, L.; Fan, M.; He, L. *Anal. Bioanal. Chem.* **2017,** *409,* 2229–2238. doi:10.1007/s00216-016-0167-8
30. Pham, X.-H.; Shim, S.; Kim, T.-H.; Hahm, E.; Kim, H.-M.; Rho, W.-Y.; Jeong, D. H.; Lee, Y.-S.; Jun, B.-H. *BioChip J.* **2017,** *11,* 46–56. doi:10.1007/s13206-016-1107-6
31. Sun, F.; Bai, T.; Zhang, L.; Ella-Menye, J.-R.; Liu, S.; Nowinski, A. K.; Jiang, S.; Yu, Q. *Anal. Chem. (Washington, DC, U. S.)* **2014,** *86,* 2387–2394. doi:10.1021/ac4040983
32. Sun, X.; Stagon, S.; Huang, H.; Chen, J.; Lei, Y. *RSC Adv.* **2014,** *4,* 23382. doi:10.1039/c4ra02423k
33. Su, H.; Wang, Y.; Yu, Z.; Liu, Y.; Zhang, X.; Wang, X.; Sui, H.; Sun, C.; Zhao, B. *Spectrochim. Acta, Part A* **2017,** *185,* 336–342. doi:10.1016/j.saa.2017.05.068
34. Gebavi, H.; Ristić, D.; Baran, N.; Mikac, L.; Mohaček-Grošev, V.; Gotić, M.; Ivanda, M. *Silicon* **2018,** *10,* 1–7. doi:10.1007/s12633-018-9906-0
35. Su, H.; Wang, Y.; Yu, Z.; Liu, Y.; Zhang, X.; Wang, X.; Sui, H.; Sun, C.; Zhao, B. *Spectrochim. Acta, Part A* **2017,** *185,* 336–342. doi:10.1016/j.saa.2017.05.068
36. Zhang, M.-L.; Fan, X.; Zhou, H.-W.; Shao, M.-W.; Zapien, J. A.; Wong, N.-B.; Lee, S.-T. *J. Phys. Chem. C* **2010,** *114,* 1969–1975. doi:10.1021/jp902775t
37. Kara, S. A.; Keffous, A.; Giovannozzi, A. M.; Rossi, A. M.; Cara, E.; D'Ortenzi, L.; Sparnacci, K.; Boarino, L.; Gabouze, N.; Soukane, S. *RSC Adv.* **2016,** *6,* 93649–93659. doi:10.1039/c6ra20323j
38. Pallas, N. R.; Harrison, Y. *Colloids Surf.* **1990,** *43,* 169–194. doi:10.1016/0166-6622(90)80287-e
39. Adamson, A. W.; Gast, A. P. *Physical chemistry of surfaces,* 6th ed.; John Wiley & Sons, Inc.: New York, NY, U.S.A., 1997.
40. Bowen, J.; Rossetto, H. L.; Kendall, K. *Surf. Topogr.: Metrol. Prop.* **2016,** *4,* 034001. doi:10.1088/2051-672x/4/3/034001

41. Pérez-Mayen, L.; Oliva, J.; De la Rosa Cruz, E. Selection criteria for SERS substrates. In *Latin America Optics and Photonics Conference,* Cancun, Mexico, Nov 16–21, 2014; OSA Publishing, 2014; LM4A.40. doi:10.1364/laop.2014.lm4a.40
42. DelRio, F. W.; de Boer, M. P.; Phinney, L. M.; Bourdon, C. J.; Dunn, M. L. Van der Waals and Capillary Adhesion of Microelectromechanical Systems. In *ASME 2006 International Mechanical Engineering Congress and Exposition,* Chicago, Illinois, USA, Nov 5–10, 2006; IMECE2006-15169. doi:10.1115/imece2006-15169
43. Kovacs, G. J.; Loutfy, R. O.; Vincett, P. S.; Jennings, C.; Aroca, R. *Langmuir* **1986,** *2,* 689–694. doi:10.1021/la00072a001

BEILSTEIN JOURNAL OF NANOTECHNOLOGY

Gas sensing properties of individual SnO_2 nanowires and SnO_2 sol–gel nanocomposites

Alexey V. Shaposhnik[1], Dmitry A. Shaposhnik[1], Sergey Yu. Turishchev[2], Olga A. Chuvenkova[2], Stanislav V. Ryabtsev[2], Alexey A. Vasiliev[*3], Xavier Vilanova[4], Francisco Hernandez-Ramirez[5] and Joan R. Morante[6]

Full Research Paper

Open Access

Address:
[1]Voronezh State Agrarian University, Michurina, 1, Voronezh, 394087, Russia, [2]Voronezh State University, Universitetskaya, 1, Voronezh, 394018, Russia, [3]NRC Kurchatov Institute, Kurchatov Sq. 1, 123182, Moscow, Russia, [4]Rovira i Virgili University, Av. Paisos Catalans 17-19, 43007, Tarragona, Spain, [5]World Sensing, S.L., Viriat 47, 10th floor, 08014 Barcelona, Spain, and [6]Catalonia Institute for Energy Research, Sant Adrià de Besòs, Catalonia, Barcelona, 08019, Spain

Email:
Alexey A. Vasiliev[*] - a-a-vasiliev@yandex.ru

* Corresponding author

Keywords:
gas sensors; gas transport method; nanowires; quasi-one-dimensional materials; sol–gel synthesis; tin dioxide; X-ray absorption near edge structure (XANES); X-ray photoelectron spectroscopy (XPS)

Beilstein J. Nanotechnol. **2019,** *10,* 1380–1390.
doi:10.3762/bjnano.10.136

Received: 14 February 2019
Accepted: 27 June 2019
Published: 08 July 2019

This article is part of the thematic issue "Chemical sensors based on quasi-one-dimensional nanostructured materials".

Guest Editor: D. Zappa

Abstract

This work is an investigation of the properties of semiconductor materials based on metal oxides, their catalytic properties, and their application as gas sensors, which were shown to exhibit high sensitivity, stability, and selectivity to target gases. The aim of this work is the comparison of gas sensing properties of tin dioxide in the form of individual nanowires and nanopowders obtained by sol–gel synthesis. This comparison is necessary because the traditional synthesis procedures of small particle, metal oxide materials seem to be approaching their limit. Because of this, there is increasing interest in the fabrication of functional materials based on nanowires, i.e., quasi-one-dimensional objects. In this work, nanocrystalline tin dioxide samples with different morphology were synthesized. The gas-transport method was used for the fabrication of well-faceted wire-like crystals with diameters ranging between 15–100 nm. The sol–gel method allowed us to obtain fragile gels from powders with grain sizes of about 5 nm. By means of X-ray photoelectron spectroscopy (XPS) it was proven that the nanowires contain considerably smaller amounts of hydroxy groups compared to the nanopowders. This leads to a decrease in the parasitic sensitivity of the sensing materials to humidity. In addition, we demonstrated that the nanowires are characterized by a nearly single-crystalline structure, ensuring higher stability of the sensor response due to the unlikelihood of sample recrystallization. The results from the ammonia detection experiments showed that the ratio of the sensor response to the surface area exhibits similar values for both the individual nanowire and nanopowders-based sensor materials.

Introduction

Semiconductor sensor functionality relies on heterogeneous catalytic chemical processes, which makes the surface-to-volume ratio of gas sensing materials an important parameter in determining their gas sensitivity. Traditionally, quasi-0-dimensional (i.e., spherical) nano-objects have been used in order to create highly porous materials. In gas sensors, agglomerates of nanoparticles with a high specific area and high surface-to-volume ratio, obtained by sintering, are traditionally used as sensing materials. By means of preparation methods such as magnetron sputtering, laser ablation, and pulverization, layer-by-layer nanoparticle deposition can be achieved with adhesion to the substrate and to previously formed material. Sol–gel processes comprise the synthesis of nanopowders, consisting of spherical nanoparticles, the preparation of pastes from these powders, and finally, deposition and annealing.

The development of the sol–gel synthesis of small particle semiconductor materials is no longer a mainstream process in sensor development, because researchers have reached the limits of this method. For this reason, the interest in the development of nanowire devices (i.e., quasi-1-dimensional objects) has increased. Their surface-to-volume ratio can be as high as that of nanopowders obtained from spherical nanoparticles.

The first nanowires were synthesized in the 1960s, but their widespread application only started in the beginning of the 21st century, when advancements in technology required the development of a wide range of nanomaterials and new methods for their treatment. The basic method for nanowire synthesis was developed and reported in detail in the classic work of R. Wagner and W. Ellis [1]. Recently, with the use of this method, SnO_2, In_2O_3, WO_3, ZnO and other metal oxide nanowires were obtained [1-5]. Liquid phase synthesis methods have also been widely implemented [6-9].

The use of metal oxide nanowires as sensing elements in gas sensors continues along two directions: The first direction involves the use of large quantities of nanowires or "nanosponge". For example, nanowires can be grown on the surface of metallic electrodes deposited on a dielectric substrate, wherein random electrical contact between wires located on different electrodes are formed. The contact between each pair of nanowires is not stable, but due to the large number of contacts, completely stable electrical contact behavior is observed (on a statistical average). Sensors based on such systems show high sensitivity [10-20]. Hierarchical structures with SnO_2 nanowires covered with additional nanoscale objects can be used for the improvement of electrical contacts [11,16,17]. A second direction in nanowire sensor development is the manufacturing of electrical contacts with individual nanowires [21-33]. These contacts can be made by means of photolithography, but more often, focused ion beam (FIB) technology is used for this purpose. This approach has several advantages: first, a reliable electrical contact between the nanowires and electrodes is provided; secondly, the possibility for the manufacture of devices with ultralow energy consumption opens up.

In the case of individual nanowires, two pairs of electrodes are deposited onto the nanowire. The outer pair is used for applying electrical heater current, while the inner pair is used for the measurement of the electrical potential drop. This 4-electrode scheme of electrical resistance measurement improves the quality of sensor response detection.

In spite of the large number of works dedicated to the use of nanowires as conductometric gas sensors, these have not been compared in detail with classical semiconductor sensors manufactured by means of the sol–gel method. Some results related to this comparison obtained by Dr. Dmitry Shaposhnik were used in his PhD thesis performed under the supervision of Professor X. Vilanova at the University Rovira I Virgili (Tarragona, Spain). The preliminary results concerning this publication were discussed at Eurosensors conferences [32,33]. The present work presents a comparative study of the material properties of SnO_2 devices prepared by different methods and by using ammonia as a reference gas for the assessment of their sensing characteristics. The use of ammonia in recent works is due to the strong interest in this gas as a marker for stomach diseases and to our collaboration with a company producing suitable measurement instruments in Russia (St. Petersburg).

Experimental

Material synthesis and characterization

SnO_2 nanowire synthesis

The gas transport method based on the vapor–liquid–solid (VLS) mechanism was used for the synthesis of SnO_2 nanowires. Argon saturated with water vapor served as the transport medium. Water was used as a mild oxidant of metallic tin in the following reaction:

$$\mathrm{Sn} + 2\mathrm{H_2O} \rightarrow \mathrm{SnO_2} + 2\mathrm{H_2} \quad (1)$$

The formation of SnO_2 is a result of a cascade of oxidation processes. It is necessary to note that in addition to the completely oxidized form of Sn (SnO_2), in gas flow there are products of the incomplete oxidation of tin, for example, SnO. On the substrate, this oxide decomposes following a disproportionation reaction as

$$2\ \mathrm{SnO} \rightarrow \mathrm{Sn} + \mathrm{SnO_2} \quad (2)$$

Metallic tin forms on the surface nanodrops, dissolving tin dioxide and the products of the incomplete oxidation of tin (SnO, Sn_2O_3, Sn_3O_4) from the argon flow. This dissolution leads finally to the saturation of tin with tin dioxide that is stable at high temperature. After this saturation occurs, the thin dioxide nanowires begin to crystallize. The diameter of the growing wires is defined by the diameter of the initial tin nanodrops. Such a process, taking place without hetero-element clusters, is called a self-catalytic process. A nanodrop of liquid metal with dissolved tin oxide is located on tip of the growing nanowire. This location will be responsible for the nanowire propagation following the VLC mechanism. This self-catalytic mechanism was described in detail in [34].

The temperature of the metal source in a tube furnace (Figure 1a) was fixed at 1100 °C. The nanowires grew on the surface of the quartz tube and on quartz substrates (Figure 1a,b). The diameter of the nanowires ranged between 15 and 150 nm (Figure 1c).

SnO_2 nanopowder synthesis

The precipitation method, reported in [30], was used to synthesize nanodispersed tin dioxide. Tin(II) acetate was dissolved in glacial acetic acid. A surplus of hydrogen peroxide was added to the solution:

$$\mathrm{Sn(CH_3COO)_2 + H_2O_2 + 2CH_3COOH \rightarrow Sn(CH_3COO)_4 + 2H_2O} \quad (3)$$

where $NH_3{\cdot}H_2O$ was added dropwise to cause hydrolytic precipitation of tin oxide as follows:

$$\mathrm{Sn(CH_3COO)_4 + 4NH_3 + 3H_2O \rightarrow H_2SnO_3 \downarrow + 4CH_3COONH_4} \quad (4)$$

The obtained colloid was precipitated by centrifugation, dried and annealed. Tin dioxide nanopowder was formed as a result of tin acid calcination as follows:

$$\mathrm{H_2SnO_3 \rightarrow SnO_2 + H_2O} \quad (5)$$

Figure 2 shows a TEM image of the obtained material. The particle diameter derived from this measurement was found to be 4–6 nm.

X-ray spectroscopy of the materials

In the present study, we used the non-destructive techniques, X-ray photoelectron spectroscopy (XPS) and X-ray absorption near edge structure (XANES), both employing the high-bril-

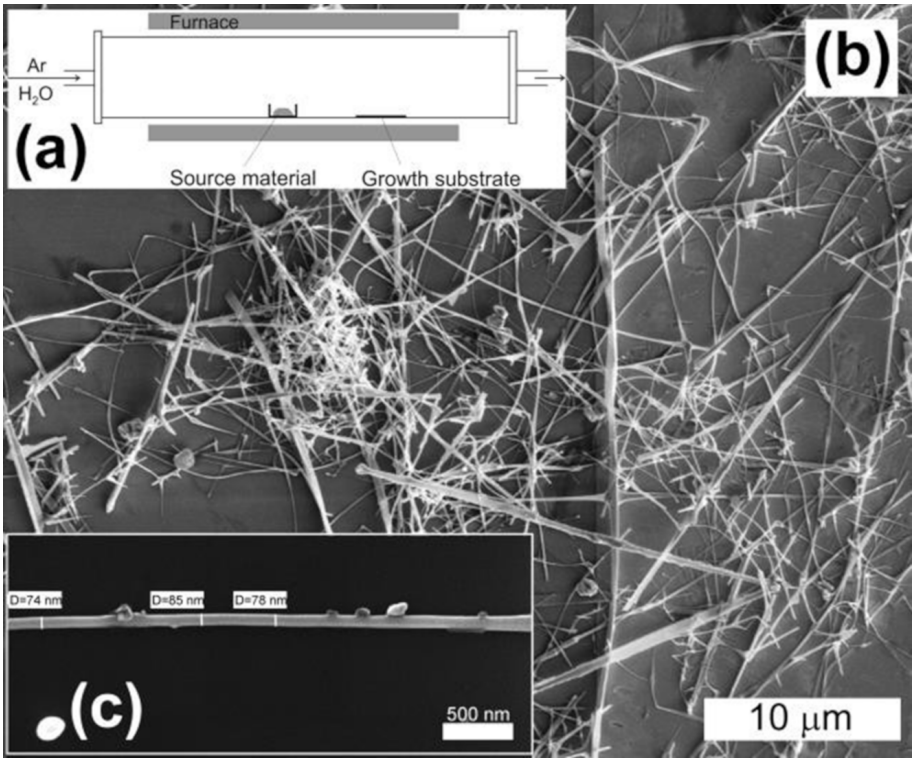

Figure 1: Scheme of nanowire synthesis (a), SEM image of SnO_2 nanowires after synthesis (b), SEM image of a single SnO_2 nanowire (c).

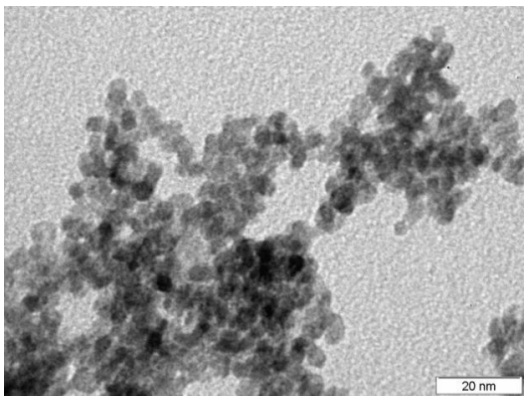

Figure 2: TEM image of blank tin dioxide nanopowder after annealing.

liance synchrotron radiation of the BESSY II storage ring at the Helmholtz Zentrum Berlin on the joint Russian–German beamline. The efficiency of XPS and XANES has previously been demonstrated in investigations of local atomic surroundings, specifically in nanomaterials, and particularly in the investigation of the structure of tin–oxygen systems [35-39]. These methods, in particular, demonstrated high sensitivity to the physical and chemical states of surfaces and interfaces. A sintered lump of tetragonal SnO_2 (Alfa Aesar) was used as a reference.

The application of synchrotron radiation allowed the variation of X-ray quantum energies for the excitation of XANES spectra. These spectra represent local partial densities of free electronic states in the conduction band of the investigated materials [35-41]. The fine structure excited by ultrasoft X-ray (synchrotron) quanta close to a given atom's core level absorption resonance has a very developed fine structure with all its features related to the density of electronic states. This at least allows for qualitative experimental information about the composition and the structure of the material surface layer to be obtained, sometimes accompanied by ab initio calculations [41,42]. According to the dipole selection rules Sn $M_{4,5}$ (3d) XANES spectra represent transitions from core 3d states to free p- and f-states in the conduction band. Oxygen K (1s) spectra in turn represent transitions from the core 1s states of oxygen atoms to the free p-states in the conduction band.

XPS is a direct experimental technique allowing the detection of the charge state of the atoms. High energy resolution XPS spectra of core level chemical shifts can give information about chemical binding energy contributions in surface layers with complex phase compositions [43-47]. In the present study, we investigated core 1s states of oxygen atoms and core 3d states of tin atoms with high resolution provided by monochromatized synchrotron radiation. The spin–orbit splitting of tin 3d core levels gives us the possibility to detect Sn $3d_{5/2}$ states with high resolution.

The application of high intensity synchrotron radiation provides high-resolution signal detection from small samples with XANES and XPS methods using photon fluxes of 10^{12}–10^{13} photons/sec at ring currents of 150–300 mA. The instrumental broadening was ≈0.1 eV. The pressure in the experimental and preparation chambers of the Russian–German lab end-station was $\approx 10^{-10}$ Torr.

The XPS analysis layer depth under 800 eV synchrotron radiation quanta (maximal flux) is estimated to be ≈1.5 nm [48].

In the case of XANES measurements, the analysis layer depth was ≈10 nm [49]. Calibration and normalization of the measured spectra was carried out using the signals from a pure gold film. Additionally, the positions of the core levels were controlled by the position of the C 1s level of the hydrocarbon contamination on the sample surfaces.

Device manufacture

Manufacture of the device based on a single nanowire

Individual nanowires were electrically contacted by direct focused-ion beam (FIB) platinum deposition, using an FEI dual beam Strata 235 instrument combined with a metal–organic injector to deposit platinum, following a process described elsewhere (Figure 3) [29]. The electrical measurements were performed using a Keithley 2400 source meter unit (SMU). For gas sensing experiments, the devices were placed in a Linkam chamber with an integrated heater; the gas flow (≥99.999% purity) was regulated by mass flow controllers.

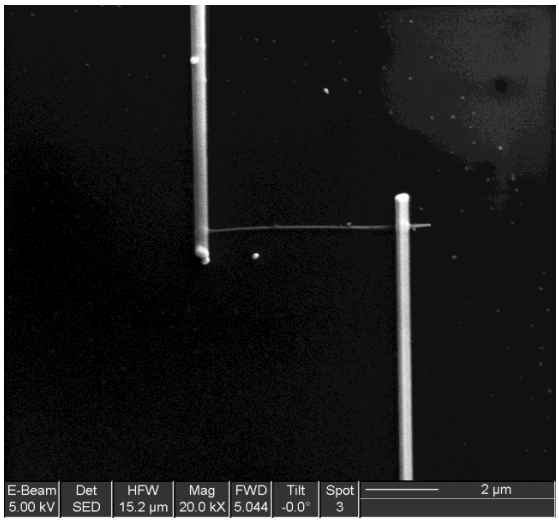

Figure 3: Nanowire with electrical contacts.

Manufacture of the device based on sol–gel material

Tin dioxide nanopowder was mixed with ethylene glycol to obtain a paste which was deposited on a thin alumina substrate with predeposited platinum electrodes using a dispenser. The thickness of the sensing layer was of 10–12 μm. After drying at 90 °C for 1 hour, the substrate was heated to 750 °C for 15 minutes and kept thereafter at 400 °C for several hours. The measurements were carried out in a special chamber integrated together with a specially designed multichannel measuring device.

Results and Discussion

X-ray spectroscopy: Comparison of nanowire and nanopowder properties

XRD spectra obtained by different methods (Figure 4) show a principal difference between the nanowires obtained by gas transport synthesis and the samples precipitated from nanopowder. The spectral band width at half-height characterizes the size of the coherence area, which is determined by the crystallinity of the structure. Nanowires formed by the vapor–liquid–solid mechanism have high and narrow peaks, confirming their monocrystalline structure. In contrast, the nanopowders exhibit low and wide peaks, demonstrating their disordered structure.

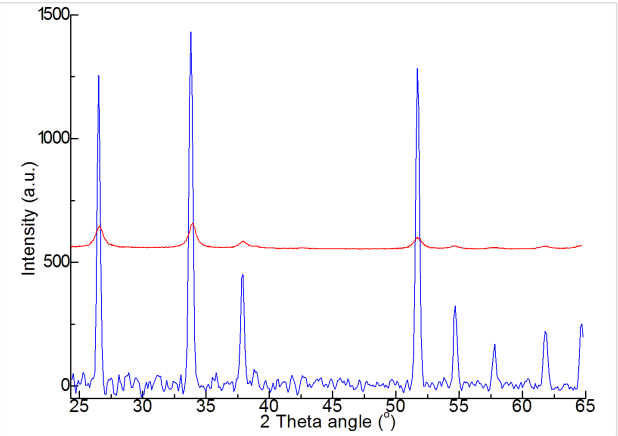

Figure 4: Experimental diffractograms of SnO2 nanowire (blue) and SnO2 nanopowder (red).

On the one hand, the disordered structure of the powder should lead to the appearance of large numbers of adsorption centers on the surface of the gas sensing material, thus increasing its sensing response. On the other hand, the monocrystallinity of the nanowires is a feature that increases the device stability.

Synchrotron study of the nanowire and nanopowder samples

The photoelectron survey spectra of SnO_2 nanowires and SnO_2 powder are given in Figure 5. All characteristic core levels of tin and oxygen atoms are marked together with the C 1s states of carbon groups. The purity of the samples is confirmed by the absence of impurity element lines. The position and single-component structure of the C 1s line for the nanowire sample is typical of the usual hydrocarbon contamination of ambient-stored samples. On powder samples, the same line exhibits a more complex fine structure as different forms of amorphous carbon are formed during material calcination.

Figure 6 represents core Sn $3d_{5/2}$ (left) and O 1s (right) lines of the samples. The binding energy for the $3d_{5/2}$ tin and oxygen 1s lines in the SnO_2 reference occurred at 487.1 eV and 531.1 eV, respectively. In the powder sample (SnO_2 pwd) the binding

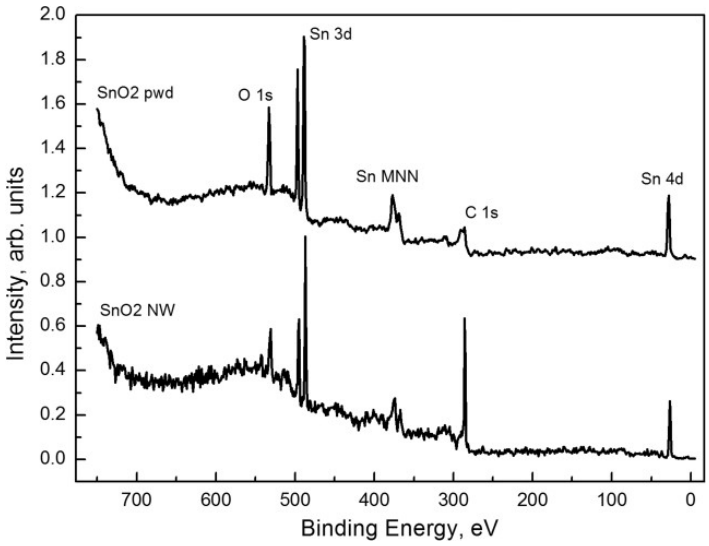

Figure 5: Photoelectron survey spectra for tin dioxide nanowires and powder samples obtained at an excitation energy of 800 eV.

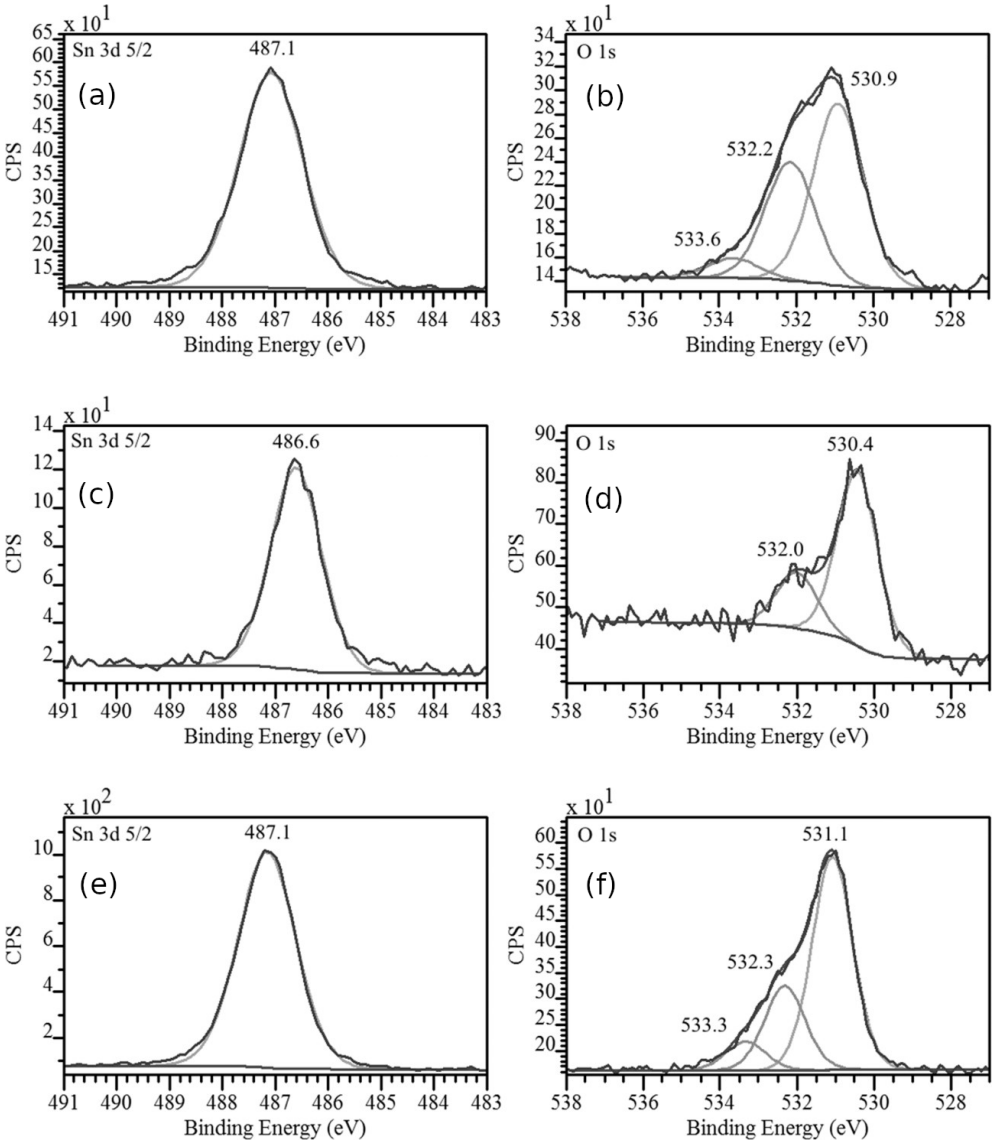

Figure 6: XPS spectra of (a) SnO_2 powder, Sn $3d_{5/2}$; (b) SnO_2 powder, O 1s; (c) SnO_2 nanowires, Sn $3d_{5/2}$; (d) SnO_2 nanowires, O 1s; (e) SnO_2 sintered lump, Sn $3d_{5/2}$; (f) SnO_2 sintered lump, O 1s.

energy was in good agreement with the binding energy in the reference sample (487.1 and 530.9 eV, respectively). The core level binding energy in the wire sample was at lower values of 486.6 (Sn $3d_{5/2}$) and 530.4 (O 1s). These values were also observed on natural oxides formed on pure metallic tin surfaces (486.6 and 530.5 eV) [38,47]. These results are also in good agreement with previously published information about VLS grown tin dioxide nanowires with well-developed surfaces and physico-chemical states [38]. High energy components are observed for the 1s line of oxygen in the range of 532.0–533.6 eV (Figure 6). These components are usually caused by hydroxy groups and water molecules [38,47,50,51] adsorbed on the surfaces of the nanosized objects under study. The fine structure of the oxygen 1s level is considerably different for tin dioxide nanowires and for powder samples; this difference can be related to the contributions from the sorbed components. The O 1s component at 532 eV binding energy, prevailing on wire-like sample surfaces, was previously observed on metallic tin foil surfaces stored under laboratory conditions [38] and for magnetron sputtered tin nanolayers oxidized in air [47]. This component is also observed on the surfaces of nanopowder particles (see Figure 6) at about 532.2 eV and believed to be typical of sorbed OH^- ions [50]. These sorption processes are more noticeable in powder particles because the O 1s component, related to oxygen atoms bound with tin (530.4 eV), is a factor of two higher than for oxygen bound in OH^- ions (≈532 eV).

The SnO_2 nanowire sample, in comparison, showed the same component ratio as the SnO_2 powder sample. Finally, the surface of the SnO_2 powder sample contains water molecules; this follows from the low relative intensity of the 533.6 eV component (Figure 6) of the O 1s line [51]. Previously, this component was observed on polycrystalline nanolayers formed by magnetron sputtering of tin and ambient air oxidation afterwards [47].

Figure 7 compares XANES Sn $M_{4,5}$ spectra of the samples with those obtained on the SnO_2 sintered lump reference sample. From the analysis of the spectra fine structure, we can conclude that the wire-like sample is closer to the reference spectrum with a more pronounced Sn $M_{4,5}$ absorption edge fine structure. Also, more noticeable is the "vacancy" feature at ≈487.5 eV observed in SnO_2 nanowires, which is usually connected with the presence of oxygen vacancies [35,37,38]. The decrease in the half-widths and the increase in the relative intensity of the peaks for each of the features observed around 490 eV (main absorption edge of the SnO_2) provides evidence for a more ordered structure in VLS grown single crystals of SnO_2 nanowires than in calcinated and partially disoriented particles in powder samples.

In the SnO_2 powder sample, a decrease is observed between the main Sn $M_{4,5}$ XANES spectrum maxima and the more developed "vacancy" feature (≈487 eV). This smearing of the fine structure density of states is typical of native SnO_{2-x} oxide covering the surface of pure metallic tin foils [37,38] and was confirmed for SnO_2 powder samples by the presence of noticeable amounts of oxygen vacancies (Figure 7).

XANES oxygen lines near K-edge spectra are presented in Figure 8. The fine structure distribution of the XANES O K spectra generally confirms the information obtained from tin absorption edge analysis. The relatively wider O K XANES spectra for the nanopowder in comparison to the SnO_2 nanowire sample is caused by the better atomic ordering in wire-like single crystals and the less compact packing of SnO_2 lattices in powder particles.

The XANES and XPS results do not contradict each other. The analysis depth of Sn $M_{4,5}$ XANES is ≈10 nm, which is much larger than the Sn $3d_{5/2}$ XPS analysis depth (<2 nm at 800 eV synchrotron photon energy). It is clear that the inner parts of the SnO_2 nanowires (Figure 7) consist of single crystals. These crystals have a very large surface, which can be similar to natural tin dioxide (see XPS data). At the same time, it is possible to assume the formation of core–shell structures in the case of SnO_2 powder samples. Due to their special formation process, powder particles may contain noticeable amounts of oxygen vacancies in their volume. This assumption moves the electronic structure of SnO_2 powder particles close to the bulk (core) of natural SnO_{2-x} oxides as confirmed by the XANES Sn $M_{4,5}$ results (see Figure 7). After calcination, followed by continuous exposure to ambient lab conditions, the

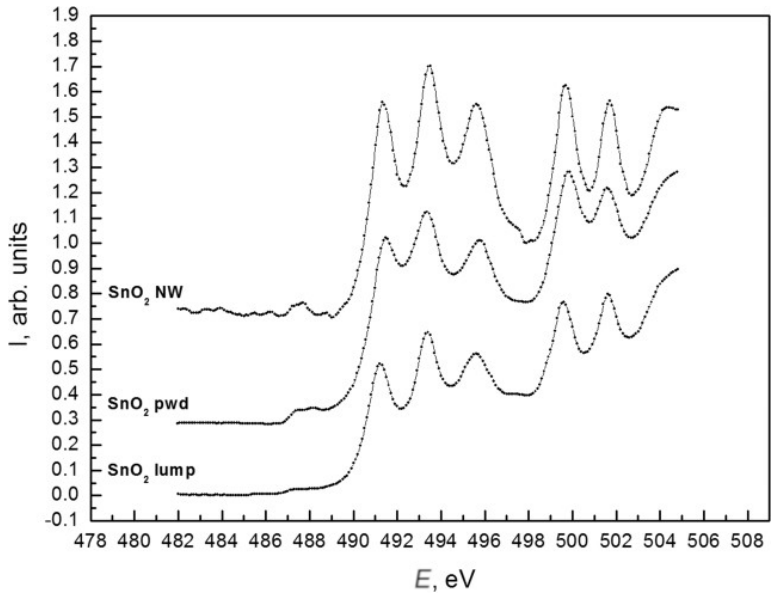

Figure 7: XANES Sn $M_{4,5}$ spectra of SnO_2 wire-like crystals (top) [37,38], SnO_2 powder (middle) and sintered SnO_2 lump reference samples (bottom).

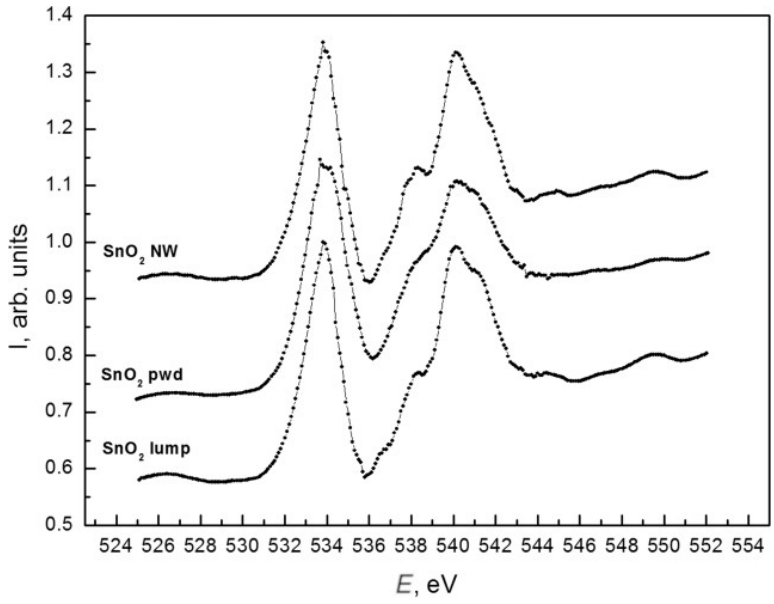

Figure 8: XANES O K spectra of SnO_2 wire-like crystals (top) [37,38], SnO_2 powder (middle) and sintered SnO_2 lump reference sample (bottom).

surface of SnO_2 powder particles appears to be covered by a thin layer (shell) containing thermally cured vacancies. According to the observed XPS data (Figure 6), this shell is ≈2 nm of SnO_2.

Thus wire-like crystals are covered by ≈1.5 nm of natural-like SnO_{2-x} while powder particles are covered by SnO_2 nanolayers of the same thickness. The bulk of the wire-like crystals consists of crystalline SnO_2. The powder particles consist of tin dioxide with the main structural unit packing character close to natural SnO_{2-x}, which means that there is a noticeable density of oxygen vacancies inside the powder particles and at the surface of wire-like crystals.

Gas sensing properties

During the characterization of the sensing properties of the devices, the following conditions were used: the sensors were exposed to air for one hour, then air was replaced by ambient conditions containing ammonia, where the sensor was also kept for one hour.

As shown in Figure 9, both sensing devices demonstrated stable readings, the background air resistance maintained a constant value, and long-term drift of the zero line was not observed. The response of the device manufactured by the sol–gel method is several times higher than that of the individual nanowire device.

The sensor response, S, is defined as the relative difference of electrical resistance:

$$S = \frac{R_0 - R_x}{R_x}, \quad (6)$$

where R_0 is the sensor resistance in air, and R_x is the resistance when exposed to ambient in the explored medium. The sensor response as a function of ammonia concentration is shown in Figure 10.

These curves can be well described by power-law functions:

$$S = a \cdot \varphi^b, \quad (7)$$

where a and b are fit parameters and φ is the gas concentration expressed in ppm (Table 1).

Table 1: parameters of power function approximation of calibration curves.

Coefficients	Nanowire		Sol–gel sensor	
	200 °C	300 °C	200 °C	300 °C
a	0.03441	0.02348	0.08121	0.09541
b	0.30905	0.36284	0.61149	0.63107

As shown in Table 1, the sensors prepared by the sol–gel technique have higher values of the coefficient a, which is responsible for the resistance. In order to understand the reasons for this behavior, the specific adsorption at the nanowire surface was estimated. This estimation was carried out considering the ge-

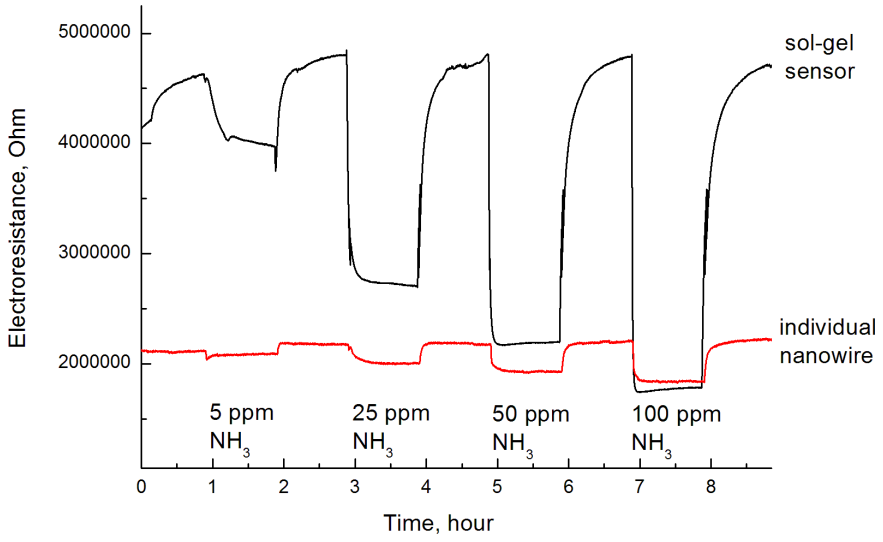

Figure 9: Response of nanowire and nanopowder sensors towards different concentrations of ammonia.

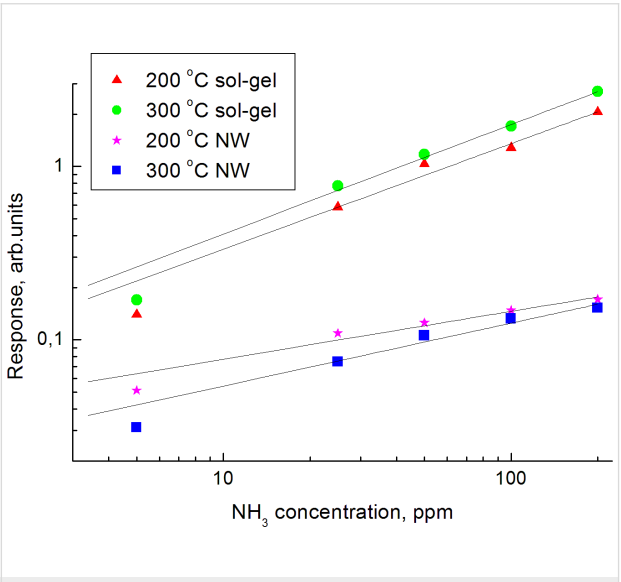

Figure 10: Calibration curves of the nanowire (NW) and sol–gel (nanopowder) sensors.

ometry of the nanowire (diameter 70 nm, length 4 μm). The tin dioxide density is ≈7 g·cm^{-3}, therefore the specific surface area is approximately 7 m^{2}g^{-1}. This is at least one order of magnitude smaller than the specific surface area of gas sensing materials obtained by the sol–gel method (≈120 m^{2}g^{-1}). The influence of the specific surface area on the sensitivity of the sensor is determined not only by the number of adsorption sites, but also by the electrical conduction mechanism. Smaller particles correspond to larger specific surface areas; the electrical conduction across such particles is more sensitive to an increase in the Debye layer width than by chemisorption.

The coefficient *b* of the power-law function also plays an important role, indicating the possibility of saturation at a high concentration of the test gas. In the sensors made by the sol–gel method, the coefficient *b* is much higher; such sensors therefore tend to saturate more easily. This phenomenon can be explained by two factors. The first one is the single crystal character of the nanowires. Uniform adsorption enthalpy of all the centers is typical of Langmuir-type adsorption, which is characterized by low power factors in the power-law approximation. Vice versa, the small size of crystallites obtained by sedimentation (Figure 2) should lead to a considerable dispersion of sorption enthalpies at the different sites. It is commonly thought that this fact results in an increase in the *b* factor. A second factor, which may lead to an increase in the *b* parameter value for sol–gel sensors is the multiplicity of current transfer routes. An increase (or decrease) of the Debye layer in individual nanowires may lead to a minimal (or maximal) current transfer. In sol–gel samples, multiple current transfer routes exist due to the percolation effect; therefore, it is almost impossible to achieve maximal or minimal values of current transfer.

As shown in Figure 11, a maximum response in both nanowire and sol–gel sensors is observed at a temperature of around 250 °C.

The effect of superficial hydroxy groups on the sensor cross-sensitivity to humidity was investigated in detail in [52]. It was shown that the application of tin dioxide materials synthesized by spark discharge and characterized as having a reduced concentration of superficial hydroxy groups resulted in a significantly decreased parasitic humidity response of the sensing ma-

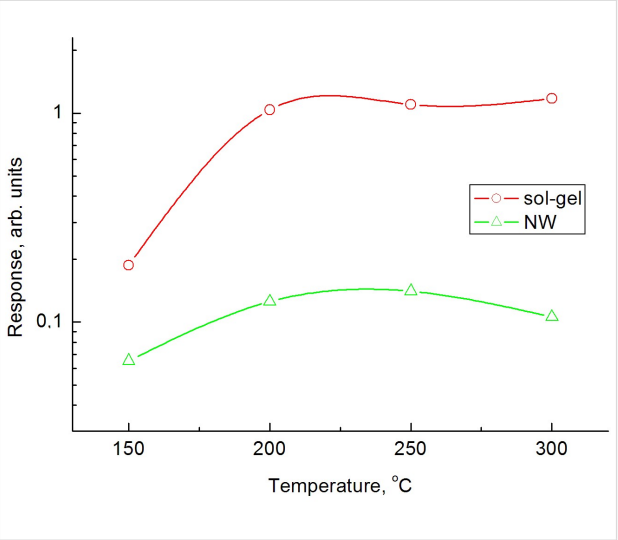

Figure 11: Response of two sensors based on sol–gel technology and on an individual nanowire (NW) as a function of sensor temperature.

terial. The same effect is observed for the tin dioxide nanowires prepared by the dry gas-transport method.

Conclusion

The presented results demonstrate that the sensors made by sol–gel technology are currently more sensitive in comparison with single-nanowire-based devices over a wide range of ammonia concentrations. Furthermore, they are simpler and cheaper to manufacture.

However, nanowire devices have also some key advantages. First, they are monocrystalline sensing materials, which provides for a greater stability in comparison with sol–gel sensors. It is known that the working surface of sol–gel sensors is continuously changing; some chemical bonds are being broken and others are being formed. This process leads to the continuous drift of sensor resistance, which distorts the signal. A monocrystalline surface is more stable, therefore resistance drift should be minimized in this case. A second advantage of individual nanowire sensors is the possibility of energy consumption reduction of the device when using a 4-electrode connection, where the outer pair of electrodes is used for applying the electrical potential. Another feature is the ability to use silicon technology for sensing device integration with measuring circuits. This allows the fabrication of an “e-nose” device in one chip.

Acknowledgements

The reported study was funded by RFBR according to the research project No. 18-29-24128. S.R., O.C. and S.T. (synchrotron studies and results discussion) acknowledge the Ministry of Education and Science of Russia, State Task for Higher Education Organizations in Science for 2017–2019, project 16.8158.2017/8.9, RFBR and Government of Voronezh Region under project 16-42-360612 pa.

ORCID® iDs

Alexey V. Shaposhnik - https://orcid.org/0000-0002-1214-2730
Dmitry A. Shaposhnik - https://orcid.org/0000-0002-3164-2108
Sergey Yu. Turishchev - https://orcid.org/0000-0003-3320-1979
Olga A. Chuvenkova - https://orcid.org/0000-0001-5701-6909
Stanislav V. Ryabtsev - https://orcid.org/0000-0001-7635-8162
Alexey A. Vasiliev - https://orcid.org/0000-0002-7416-1638

References

1. Wagner, R. S.; Ellis, W. C. *Appl. Phys. Lett.* **1964,** *4,* 89–90. doi:10.1063/1.1753975
2. Givargizov, E. I. *Krist. Tech.* **1975,** *10,* 473–484. doi:10.1002/crat.19750100503
3. Wang, Z. L. *Annu. Rev. Phys. Chem.* **2004,** *55,* 159–196. doi:10.1146/annurev.physchem.55.091602.094416
4. Zhu, Z.; Chen, T.-L.; Gu, Y.; Warren, J.; Osgood, R. M. *Chem. Mater.* **2005,** *17,* 4227–4234. doi:10.1021/cm050584+
5. Kar, S.; Pal, B. N.; Chaudhuri, S.; Chakravorty, D. *J. Phys. Chem. B* **2006,** *110,* 4605–4611. doi:10.1021/jp056673r
6. Chang, Y.; Zeng, H. C. *Cryst. Growth Des.* **2004,** *4,* 397–402. doi:10.1021/cg034127m
7. Kunjara Na Ayudhya, S.; Tonto, P.; Mekasuwandumrong, O.; Pavarajarn, V.; Praserthdam, P. *Cryst. Growth Des.* **2006,** *6,* 2446–2450. doi:10.1021/cg050345z
8. Wang, Y.; Cao, G. *Chem. Mater.* **2006,** *18,* 2787–2804. doi:10.1021/cm052765h
9. Tong, Y.; Liu, Y.; Dong, L.; Zhao, D.; Zhang, J.; Lu, Y.; Shen, D.; Fan, X. *J. Phys. Chem. B* **2006,** *110,* 20263–20267. doi:10.1021/jp063312i
10. Kim, H. W.; Choi, S.-W.; Katoch, A.; Kim, S. S. *Sens. Actuators, B* **2013,** *177,* 654–658. doi:10.1016/j.snb.2012.11.021
11. Khoang, N. D.; Trung, D. D.; Van Duy, N.; Hoa, N. D.; Van Hieu, N. *Sens. Actuators, B* **2012,** *174,* 594–601. doi:10.1016/j.snb.2012.07.118
12. Jung, S.-H.; Choi, S.-W.; Kim, S. S. *Sens. Actuators, B* **2012,** *171–172,* 672–678. doi:10.1016/j.snb.2012.05.053
13. Hwang, I.-S.; Kim, S.-J.; Choi, J.-K.; Jung, J.-J.; Yoo, D. J.; Dong, K.-Y.; Ju, B.-K.; Lee, J.-H. *Sens. Actuators, B* **2012,** *165,* 97–103. doi:10.1016/j.snb.2012.02.022
14. Comini, E.; Sberveglieri, G. *Mater. Today* **2010,** *13,* 36–44. doi:10.1016/s1369-7021(10)70126-7
15. Shaalan, N. M.; Yamazaki, T.; Kikuta, T. *Sens. Actuators, B* **2012,** *166–167,* 671–677. doi:10.1016/j.snb.2012.03.038
16. Kwak, C.-H.; Woo, H.-S.; Lee, J.-H. *Sens. Actuators, B* **2014,** *204,* 231–238. doi:10.1016/j.snb.2014.07.084
17. Choi, S.-W.; Katoch, A.; Sun, G.-J.; Kim, S. S. *Sens. Actuators, B* **2013,** *181,* 787–794. doi:10.1016/j.snb.2013.02.010
18. Zappa, D.; Comini, E.; Zamani, R.; Arbiol, J.; Morante, J. R.; Sberveglieri, G. *Sens. Actuators, B* **2013,** *182,* 7–15. doi:10.1016/j.snb.2013.02.076
19. Comini, E.; Baratto, C.; Faglia, G.; Ferroni, M.; Vomiero, A.; Sberveglieri, G. *Prog. Mater. Sci.* **2009,** *54,* 1–67. doi:10.1016/j.pmatsci.2008.06.003

20. Vomiero, A.; Ponzoni, A.; Comini, E.; Ferroni, M.; Faglia, G.; Sberveglieri, G. *Nanotechnology* **2010,** *21,* 145502. doi:10.1088/0957-4484/21/14/145502
21. Kolmakov, A.; Klenov, D. O.; Lilach, Y.; Stemmer, S.; Moskovits, M. *Nano Lett.* **2005,** *5,* 667–673. doi:10.1021/nl050082v
22. Sysoev, V. V.; Button, B. K.; Wepsiec, K.; Dmitriev, S.; Kolmakov, A. *Nano Lett.* **2006,** *6,* 1584–1588. doi:10.1021/nl060185t
23. Shao, F.; Hoffmann, M. W. G.; Prades, J. D.; Zamani, R.; Arbiol, J.; Morante, J. R.; Varechkina, E.; Rumyantseva, M.; Gaskov, A.; Giebelhaus, I.; Fischer, T.; Mathur, S.; Hernández-Ramírez, F. *Sens. Actuators, B* **2013,** *181,* 130–135. doi:10.1016/j.snb.2013.01.067
24. Chinh, N. D.; Van Toan, N.; Van Quang, V.; Van Duy, N.; Hoa, N. D.; Van Hieu, N. *Sens. Actuators, B* **2014,** *201,* 7–12. doi:10.1016/j.snb.2014.04.095
25. Kolmakov, A.; Moskovits, M. *Annu. Rev. Mater. Res.* **2004,** *34,* 151–180. doi:10.1146/annurev.matsci.34.040203.112141
26. Sysoev, V. V.; Strelcov, E.; Sommer, M.; Bruns, M.; Kiselev, I.; Habicht, W.; Kar, S.; Gregoratti, L.; Kiskinova, M.; Kolmakov, A. *ACS Nano* **2010,** *4,* 4487–4494. doi:10.1021/nn100435h
27. Sysoev, V. V.; Strelcov, E.; Kar, S.; Kolmakov, A. *Thin Solid Films* **2011,** *520,* 898–903. doi:10.1016/j.tsf.2011.04.179
28. Hernández-Ramírez, F.; Tarancón, A.; Casals, O.; Rodríguez, J.; Romano-Rodríguez, A.; Morante, J. R.; Barth, S.; Mathur, S.; Choi, T. Y.; Poulikakos, D.; Callegari, V.; Nellen, P. M. *Nanotechnology* **2006,** *17,* 5577–5583. doi:10.1088/0957-4484/17/22/009
29. Hernández-Ramírez, F.; Tarancón, A.; Casals, O.; Arbiol, J.; Romano-Rodríguez, A.; Morante, J. R. *Sens. Actuators, B* **2007,** *121,* 3–17. doi:10.1016/j.snb.2006.09.015
30. Shaposhnik, D.; Pavelko, R.; Llobet, E.; Gispert-Guirado, F.; Vilanova, X. *Sens. Actuators, B* **2012,** *174,* 527–534. doi:10.1016/j.snb.2012.05.028
31. Shaposhnik, D. Determination of hydrogen-containing gases in air with SnO_2-based sensors. Ph.D. Thesis, University Rovira i Virgili, Tarragona, Spain, 2015.
32. Shaposhnik, A.; Ryabtsev, S.; Shao, F.; Hernandez-Ramirez, F.; Morante, J.; Zviagin, A.; Meshkova, N.; Shaposhnik, D.; Vasiliev, A. *Procedia Eng.* **2012,** *47,* 1398–1401. doi:10.1016/j.proeng.2012.09.418
33. Shaposhnik, A.; Ryabtsev, S.; Shao, F.; Hernandez-Ramirez, F.; Morante, J.; Zviagin, A.; Sizask, E.; Shaposhnik, D. *Procedia Eng.* **2014,** *87,* 951–954. doi:10.1016/j.proeng.2014.11.314
34. Zanotti, L.; Zha, M.; Calestani, D.; Comini, E.; Sberveglieri, G. *Cryst. Res. Technol.* **2005,** *40,* 932–936. doi:10.1002/crat.200410462
35. Baumann, T. F.; Kucheyev, S. O.; Gash, A. E.; Satcher, J. H. *Adv. Mater. (Weinheim, Ger.)* **2005,** *17,* 1546–1548. doi:10.1002/adma.200500074
36. Zhou, J. G.; Fang, H. T.; Maley, J. M.; Ko, J. Y. P.; Murphy, M.; Chu, Y.; Sammynaiken, R.; Sham, T. K. *J. Phys. Chem. C* **2009,** *113,* 6114–6117. doi:10.1021/jp810639y
37. Chuvenkova, O. A.; Domashevskaya, E. P.; Ryabtsev, S. V.; Vysotskii, D. V.; Popov, A. E.; Yurakov, Y. A.; Vilkov, O. Y.; Ovsyannikov, R.; Appathurai, N.; Turishchev, S. Y. *J. Surf. Invest.: X-Ray, Synchrotron Neutron Tech.* **2014,** *8,* 111–116. doi:10.1134/s102745101401025x
38. Chuvenkova, O. A.; Domashevskaya, E. P.; Ryabtsev, S. V.; Yurakov, Y. A.; Popov, A. E.; Koyuda, D. A.; Nesterov, D. N.; Spirin, D. E.; Ovsyannikov, R. Y.; Turishchev, S. Y. *Phys. Solid State* **2015,** *57,* 153–161. doi:10.1134/s1063783415010072
39. Domashevskaya, E. P.; Ryabtsev, S. V.; Yurakov, Y. A.; Chuvenkova, O. A.; Kashkarov, V. M.; Turishchev, S. Y.; Kushev, S. B.; Lukin, A. N. *Thin Solid Films* **2007,** *515,* 6350–6355. doi:10.1016/j.tsf.2006.11.092
40. Bunker, G. *Introduction to XAFS;* Cambridge University Press: Cambridge, United Kingdom, 2010. doi:10.1017/cbo9780511809194
41. Kurganskii, S. I.; Manyakin, M. D.; Dubrovskii, O. I.; Chuvenkova, O. A.; Turishchev, S. Y.; Domashevskaya, E. P. *Phys. Solid State* **2014,** *56,* 1748–1753. doi:10.1134/s1063783414090170
42. Manyakin, M. D.; Kurganskii, S. I.; Dubrovskii, O. I.; Chuvenkova, O. A.; Domashevskaya, E. P.; Ryabtsev, S. V.; Ovsyannikov, R.; Turishchev, S. Y. *Comput. Mater. Sci.* **2016,** *121,* 119–123. doi:10.1016/j.commatsci.2016.04.034
43. Hüfner, S., Ed. *Very High Resolution Photoelectron Spectroscopy;* Lecture Notes in Physics; Springer Berlin: Berlin, Germany, 2007. doi:10.1007/3-540-68133-7
44. Chen, Z.; Lai, J. K. L.; Shek, C.-H. *Appl. Phys. Lett.* **2006,** *89,* 231902. doi:10.1063/1.2399352
45. Kwoka, M.; Ottaviano, L.; Passacantando, M.; Santucci, S.; Czempik, G.; Szuber, J. *Thin Solid Films* **2005,** *490,* 36–42. doi:10.1016/j.tsf.2005.04.014
46. Babu, B.; Neelakanta Reddy, I.; Yoo, K.; Kim, D.; Shim, J. *Mater. Lett.* **2018,** *221,* 211–215. doi:10.1016/j.matlet.2018.03.107
47. Domashevskaya, E. P.; Chuvenkova, O. A.; Ryabtsev, S. V.; Yurakov, Y. A.; Kashkarov, V. M.; Shchukarev, A. V.; Turishchev, S. Y. *Thin Solid Films* **2013,** *537,* 137–144. doi:10.1016/j.tsf.2013.03.051
48. Yeh, J. J.; Lindau, I. *At. Data Nucl. Data Tables* **1985,** *32,* 1–155. doi:10.1016/0092-640x(85)90016-6
49. Erbil, A.; Cargill, G. S., III; Frahm, R.; Boehme, R. F. *Phys. Rev. B* **1988,** *37,* 2450–2464. doi:10.1103/physrevb.37.2450
50. Jerdev, D. I.; Koel, B. E. *Surf. Sci.* **2001,** *492,* 106–114. doi:10.1016/s0039-6028(01)01407-8
51. Crist, B. V. *PDF Handbook of Monochromatic XPS Spectra;* XPS International LLC, 1999; Vol. 1.
52. Vasiliev, A.; Varfolomeev, A.; Volkov, I.; Simonenko, N.; Arsenov, P.; Vlasov, I.; Ivanov, V.; Pislyakov, A.; Lagutin, A.; Jahatspanian, I.; Maeder, T. *Sensors* **2018,** *18,* 2600. doi:10.3390/s18082600

License and Terms

BEILSTEIN JOURNAL OF NANOTECHNOLOGY

High-temperature resistive gas sensors based on ZnO/SiC nanocomposites

Vadim B. Platonov[1], Marina N. Rumyantseva[*1,2], Alexander S. Frolov[1], Alexey D. Yapryntsev[3] and Alexander M. Gaskov[1,2]

Full Research Paper

Open Access

Address:
[1]Chemistry Department, Moscow State University, 1–3 Leninskie gory, Moscow, 119991 Russia, [2]Saint Petersburg State University, 7/9 Universitetskaya nab., Saint Petersburg, 199034 Russia and [3]Kurnakov Institute of General and Inorganic Chemistry of Russian Academy of Sciences, 31 Leninsky prospect, Moscow, 119991 Russia

Email:
Marina N. Rumyantseva[*] - roum@inorg.chem.msu.ru

* Corresponding author

Keywords:
electrospinning; high temperature gas sensor; n–n heterojunction; ZnO/SiC nanocomposite

Beilstein J. Nanotechnol. **2019,** *10,* 1537–1547.
doi:10.3762/bjnano.10.151

Received: 28 February 2019
Accepted: 14 June 2019
Published: 26 July 2019

This article is part of the thematic issue "Chemical sensors based on quasi-one-dimensional nanostructured materials".

Guest Editor: D. Zappa

Abstract

Increasing requirements for environmental protection have led to the need for the development of control systems for exhaust gases monitored directly at high temperatures in the range of 300–800 °C. The development of high-temperature gas sensors requires the creation of new materials that are stable under these conditions. The stability of nanostructured semiconductor oxides at high temperature can be enhanced by creating composites with highly dispersed silicon carbide (SiC). In this work, ZnO and SiC nanofibers were synthesized by electrospinning of polymer solutions followed by heat treatment, which is necessary for polymer removal and crystallization of semiconductor materials. ZnO/SiC nanocomposites (15–45 mol % SiC) were obtained by mixing the components in a single homogeneous paste with subsequent thermal annealing. The composition and microstructure of the materials were characterized by X-ray diffraction (XRD), scanning electron microscopy (SEM), Fourier-transform infrared spectroscopy (FTIR) and X-ray photoelectron spectroscopy (XPS). The electrophysical and gas sensing properties of the materials were investigated by in situ conductivity measurements in the presence of the reducing gases CO and NH_3 (20 ppm), in dry conditions (relative humidity at 25 °C RH_{25} = 0) and in humid air (RH_{25} = 30%) in the temperature range 400–550 °C. The ZnO/SiC nanocomposites were characterized by a higher concentration of chemisorbed oxygen, higher activation energy of conductivity, and higher sensor response towards CO and NH_3 as compared with ZnO nanofibers. The obtained experimental results were interpreted in terms of the formation of an n–n heterojunction at the ZnO/SiC interface.

Introduction

The risk of air pollution is growing due to the development of new technologies in the chemical, metallurgical and food industries, the use of bio-fuels in the energy sector, modern waste treatment, and new automotive and aircraft engines [1,2]. Increasing requirements for environmental protection lead to the need for the development of control systems for exhaust gases that can directly monitor at high temperatures in the range of 300–800 °C. The composition of the main components of exhaust gas includes CO_2, CO, SO_2, H_2S, NO_x, C_nH_{2n+2}, and NH_3. The ratio of these components depends primarily on the technology features and fuel type. High-temperature gas sensors are needed for local monitoring of pollution emissions, as well as for monitoring the complete combustion of fuel and controlling medium-temperature chemical and metallurgical processes [3-5]. The development of high-temperature gas sensors requires the creation of new materials that are stable at 300–600 °C, high humidity, and lack of oxygen. Nanostructured semiconductor oxides, such as SnO_2, ZnO, WO_3, and In_2O_3, that have been widely used in resistive gas sensors cannot be applied directly, primarily due to the drift of the sensor parameters at temperatures above 500 °C. The stability of nanostructured semiconductor oxides at high temperature can be enhanced by creating composite nanomaterials using highly dispersed silicon carbide (SiC). The unique physical and chemical properties of silicon carbide – wide band gap (E_g = 2.4–3.2 eV), high Debye temperature 1400 K, high thermal conductivity of 4.9 W/cm·K, low reactivity to oxygen and water vapor – ensure the stability of composite materials with respect to temperature, radiation, chemical and mechanical effects [6,7]. It has been shown that in MO/SiC nanocomposites containing metal oxide (MO) and nanostructured SiC, the presence of silicon carbide inhibits the growth of MO crystallites at high temperatures [8]. The difference in the adsorption properties, reactivity and electrical behavior of semiconductor oxides and silicon carbide, as well as possible chemical interactions on their interface, cause changes in the sensor performance of composite materials. The SiC-based materials in the form of planar Pt/MO/SiC heterostructures were intensively studied as sensitive elements of field-effect or Schottky diode gas sensors. These materials have a high sensitivity to hydrogen and hydrocarbons in the temperature range of 200–600 °C [9-14]. The resistive-type sensors based on MO/SiC composite materials have not been practically studied. A few works of the MO/SiC composite material based on highly dispersed silicon carbide [8,15] showed the stability of the material structure at 600 °C and its high response to carbon monoxide.

Electrospinning is inexpensive tool widely used today for preparation porous, ultrathin fibers of SiC and metal oxides as well as MO/SiC composites from polymer solutions [16-19]. The combination of unlimited length, highly porous microstructure, and high surface area come together to create ideal gas sensor materials.

In this work, we prepared ZnO/SiC nanocomposite materials by mixing and heat treatment of electrospun ZnO nanofibers and nanocrystalline silicon carbide of 3C-SiC polytype. The effect of silicon carbide on the structure and electrical properties of composite materials was studied using different techniques. The work is aimed at creating the resistive-type gas sensors based on ZnO/SiC composites and studying the sensor performance towards the main components of the exhaust gases CO and NH_3 in air at a temperature range of 400–550 °C.

Results and Discussion

The nanocomposite synthesis scheme is shown in Figure 1 and described in detail in the Experimental part. The characteristics of the synthesized materials are summarized in Table 1.

Figure 2 shows the scanning electron microscopy (SEM) micrographs of SiC (Figure 2a,c) and ZnO (Figure 2b,d) nanofibers in a polymer matrix (Figure 2a,b) and after annealing (Figure 2c,d). The polymeric fibers containing polycarbosilane (Figure 2a) are tapered with a width of 8–10 μm and a thickness of about 200 nm. Exposure to high temperature and pressure, which is necessary for the formation of crystalline SiC, leads to the destruction of fibers and the formation of porous powders (Figure 2c) with an average pore diameter of 30 nm (Figure 2f). The polymeric fibers containing zinc acetate (Figure 2b) are cylindrical wires about 500 nm in diameter. The ZnO nanofibers obtained after annealing (Figure 2d) consist of polycrystalline wires with an average diameter of 150 nm formed by nanocrystals about 20–30 nm in size. The average pore diameter, estimated from the data of low-temperature nitrogen adsorption, was 50 nm (Figure 2f). In the ZnO/SiC nanocomposites (Figure 2e), formed from ZnO nanofibers and SiC powder by mixing components in a single homogeneous paste with subsequent annealing at 550 °C, the quasi-one-dimensional structure of ZnO wires is retained.

The X-ray diffraction data indicate (Figure 3a) that the annealing of polymer fibers leads to the formation of crystalline phases of ZnO (wurtzite, ICDD 36-1451) and SiC (3C polytype, ICDD 29-1129). The crystallite size (d_{XRD}), estimated from the broadening of (100) ZnO and (111) 3C-SiC diffraction peaks, as determined by the Scherrer formula, is consistent with the size of crystalline particles from SEM analysis. The diffraction patterns of ZnO/SiC nanocomposites contain diffraction maxima of both crystalline phases (Figure 3b), and the intensity of the SiC peaks naturally in-

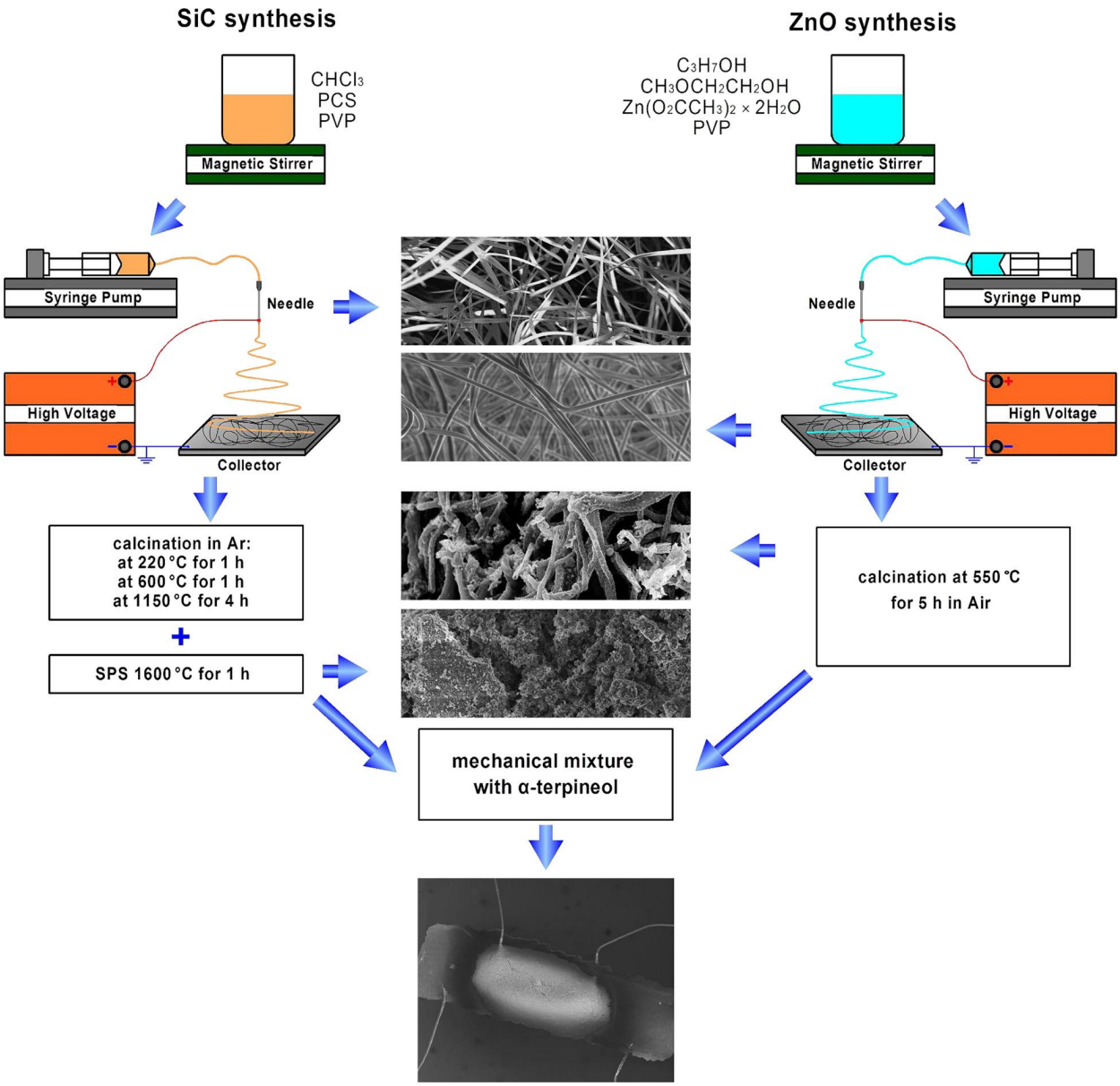

Figure 1: Synthesis scheme of nanocrystalline ZnO, SiC and ZnO/SiC nanocomposite materials.

Table 1: Microstructure characteristics and electrophysical properties of ZnO nanofibers, ZnO/SiC nanocomposites and nanocrystalline SiC powder.

Sample	C_{SiC}[a], mol %	Phase composition, XRD	d_{XRD}[b], nm	S_{BET}[c], m^2/g	R_{air}[d], Ohm (400 °C)	E_a[e], eV
ZnO	0	ZnO	18 ± 2	10 ± 1	8.6×10^5	0.40 ± 0.04
ZnO/SiC_15	15	ZnO/SiC	18 ± 2/25 ± 3	–	4.6×10^6	0.71 ± 0.06
ZnO/SiC_30	30	ZnO/SiC	18 ± 2/25 ± 3	–	7.0×10^6	0.73 ± 0.09
ZnO/SiC_45	45	ZnO/SiC	18 ± 2/25 ± 3	–	1.5×10^7	0.78 ± 0.07
SiC	100	SiC	27 ± 3	6 ± 1	8.5×10^9	–

[a]SiC content; [b]crystallite size estimated from the broadening of the (100) ZnO and (111) 3C-SiC reflections using the Scherrer formula; [c]specific surface area; [d]resistance in dry air at 400 °C; [e]activation energy of conductivity in the temperature range 400–500 °C.

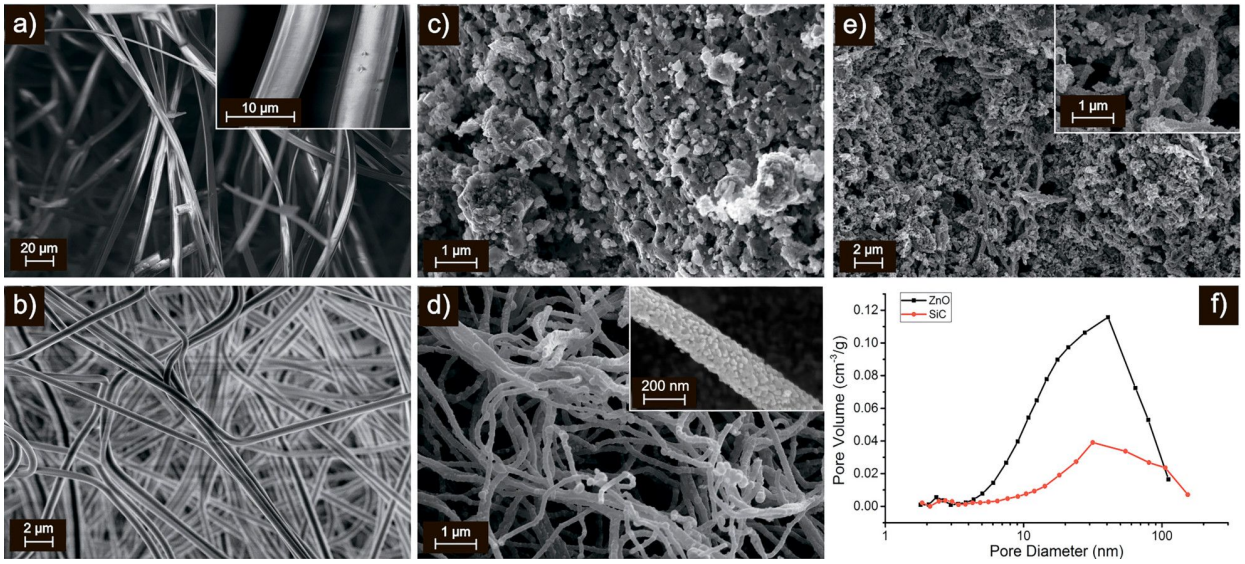

Figure 2: SEM micrographs of polymer nanofibers containing polycarbosilane (a) and zinc acetate (b). SEM micrographs of annealed SiC (c) and ZnO (d). (e) SEM micrograph of ZnO/SiC_45 nanocomposite. (f) Pore size distribution of annealed ZnO and SiC.

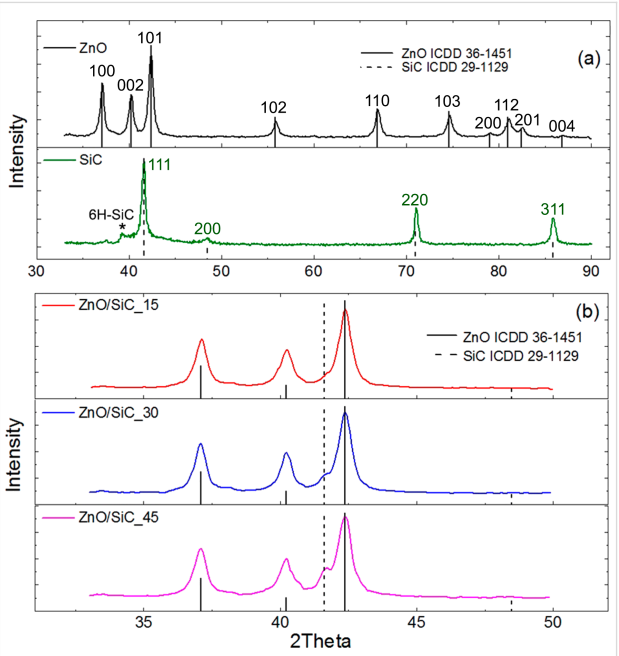

Figure 3: X-ray diffraction patterns of (a) ZnO nanofibers and nanocrystalline SiC and (b) ZnO/SiC nanocomposites. The vertical solid and dotted lines correspond to ICDD 36-1451 (ZnO, wurtzite) and ICDD 29-1129 (SiC-3C polytype) references, respectively.

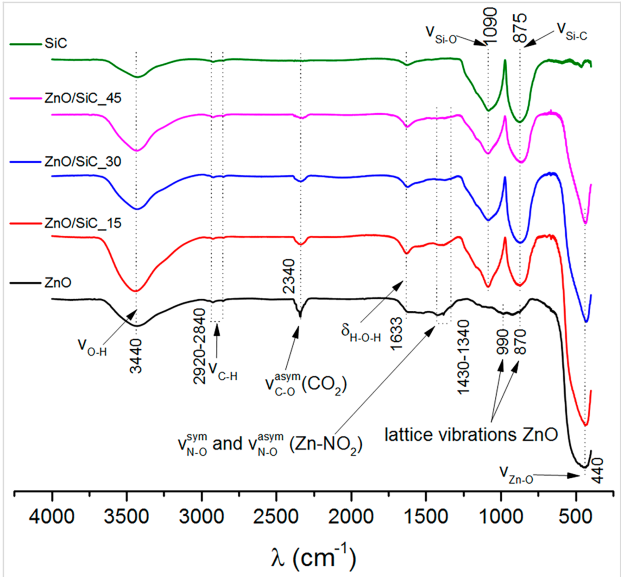

Figure 4: FTIR spectra of ZnO nanofibers, nanocrystalline SiC and ZnO/SiC nanocomposites.

creases with increasing silicon carbide content in the nanocomposites.

The study of the surface composition of the synthesized materials was carried out using FTIR and XPS methods. Figure 4 shows the IR absorption spectra of ZnO, SiC, and ZnO/SiC nanocomposites. The spectrum of zinc oxide contains an intense broad signal, corresponding to the stretching vibrations of Zn–O bonds (635–400 cm^{-1}). The above spectrum also shows the signals from the multi-phonon vibrational modes of the ZnO lattice (990 and 870 cm^{-1}). In accordance with the literature data, such oscillations do not appear at 78 K, but are noticeable at room temperature [20]. Nitro and nitrite groups [21,22] formed during the decomposition of PVP are also present on the surface of zinc oxide, as evidenced by the appearance of IR signals in the 1430–1260 cm^{-1} region, corresponding to the

symmetric and asymmetric oscillations of the N–O bond. A broad peak in the region of 3750–3000 cm^{-1} is due to the stretching vibrations of hydroxy groups on the ZnO surface. The deformation vibrations of adsorbed water molecules are recorded at 1640 cm^{-1}. In addition to these, the spectrum contains peaks related to the vibrations of the C–O bond in CO_2 molecules adsorbed on the ZnO surface (2430–2320 cm^{-1}) and C–H bonds (2920–2840 cm^{-1}) in the residues of the organic components used in the synthesis of ZnO nanofibers.

The FTIR absorption spectrum of the SiC sample contains two intense peaks with absorption maxima at 900 cm^{-1} and 1067 cm^{-1}, corresponding to the stretching vibrations of the Si–C and Si–O bonds, respectively [23]. This indicates the formation of an amorphous SiO_2 shell on the surface of SiC nanoparticles, which does not appear on the diffraction patterns of the samples. In addition to these absorption lines, the spectrum contains the signals corresponding to O–H vibrations of surface hydroxy groups, deformation vibrations of adsorbed water molecules, and C–H bonds in the residues of organic components. All these oscillations are also present in the FTIR spectra of ZnO/SiC nanocomposites with the intensity ratio corresponding to the molar ratio of ZnO and SiC. Any additional vibrational modes do not arise in the FTIR spectra of ZnO/SiC nanocomposites.

To reveal the possible interactions between SiC and ZnO nanoparticles, and to shed light on the surface composition of the materials, we used X-ray photoelectron spectroscopy (XPS). Figure 5 and Figure 6 show the XPS spectra of ZnO, SiC and the ZnO/SiC_15 nanocomposite in the Zn 2p, O 1s, Si 2p, and C 1s binding energy regions. The survey spectra are provided in Supporting Information File 1 (Figure S1). For the SiC sample, it was found that the Si 2p region contains three components at 100.6 (Si1), 103.0 (Si2), and 106.3 (Si3) eV (Figure 5a). The first one corresponds to silicon carbide, while the second one refers to silicon oxide [24]. A weak third component may be associated with Si–O_2 bonds [19]. The formation of silicon oxide is also observed in the photoelectron spectrum in the O 1s region, containing two components at 532.9 (O1) and 536 (O2) eV. The first component is assigned to the oxygen bonded to two silicon atoms [24] while the second one may be associated with the chemisorbed oxygen (Figure 5c). The presence of an Si–O component in the O 1s spectrum is consistent with the results from IR spectroscopy. The carbon in silicon carbide is also found to be oxidized. The spectrum of the C 1s region contains four components at 283.1 (C1), 285.1 (C2), 286.5 (C3), 289.3 and (C4) eV, which correspond to carbide in SiC, amorphous carbon, C–O and ether groups, respectively [24] (Figure 5b). For ZnO nanofibers and the ZnO/SiC_15 nanocomposite, the XPS spectra in the Zn 2p region depicted in

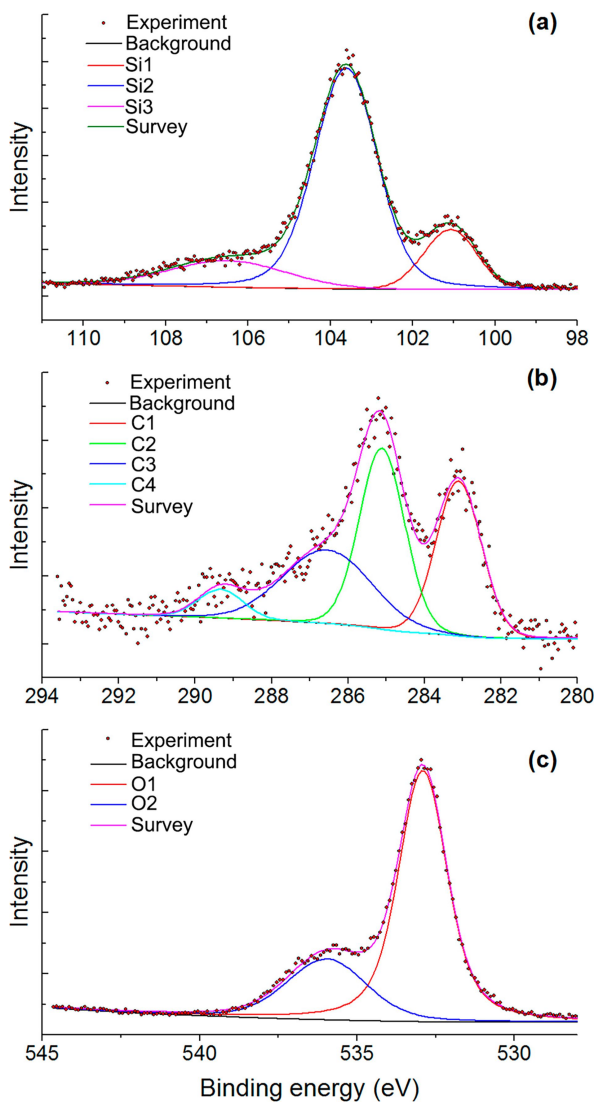

Figure 5: X-ray photoelectron spectra of SiC in the Si 2p (a), C 1s (b), and O 1s (c) regions.

Figure 6a,b contain only one component related to Zn in (+2) oxidation state. The XPS spectra in the O 1s region (Figure 6c,d) contain two components. The first one (O1) at 530.2 eV corresponds to the lattice oxygen in the ZnO phase, while the high-energy component (O2) at 531.2 eV is assigned to the different oxygen-containing species on the zinc oxide surface, which include hydroxy groups and different forms of chemisorbed oxygen [25-28]. No changes were detected in the Zn 2p XPS spectrum of ZnO/SiC nanocomposites compared with the similar spectrum of ZnO. At the same time, the ratio O1/O2 = 0.75 in the O 1s spectrum of the ZnO/SiC_15 composite is reduced as compared with that in the ZnO O 1s spectrum (O1/O2 = 0.85), which may be due to the increase in the concentration of oxygen surface species. The contribution from the Si–O component (532.9 and 536 eV, Figure 5c) in the O 1s

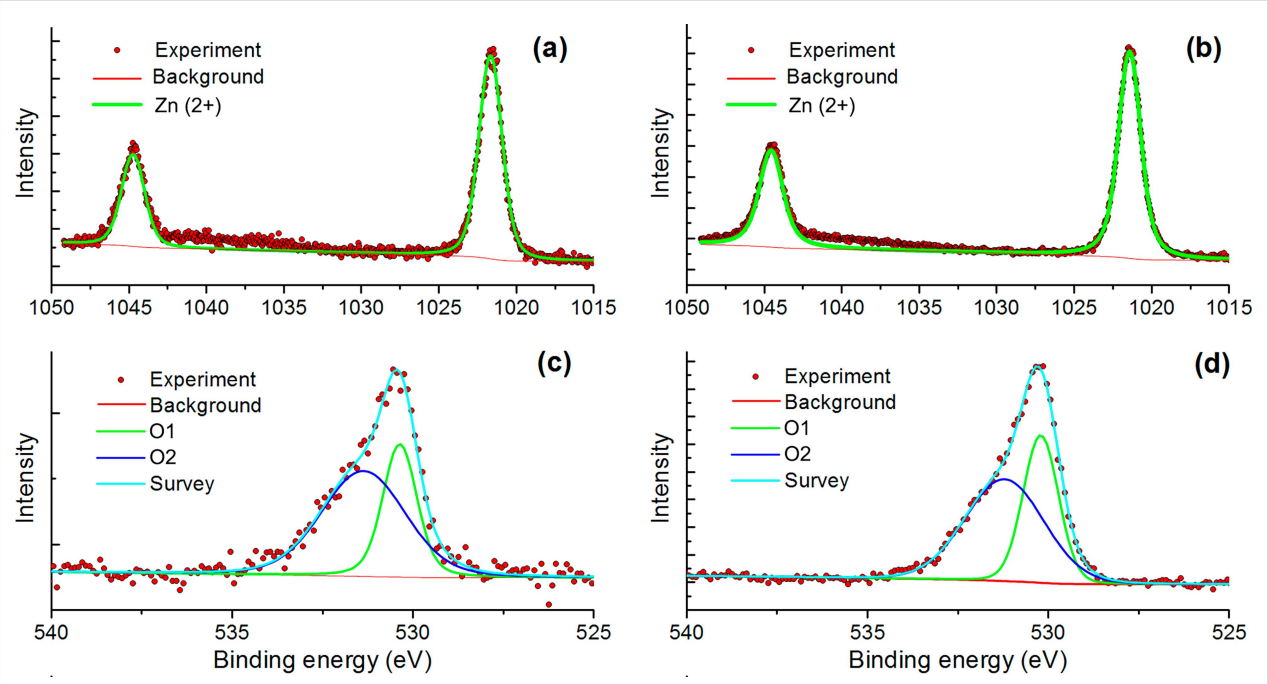

Figure 6: X-ray photoelectron spectra of the ZnO/SiC_15 nanocomposite (a, c) and ZnO nanofibers (b, d) in the Zn 2p (a, b) and O 1s (c, d) regions.

spectrum of ZnO/SiC_15 is negligible. The XPS spectrum in Si 2p region, depicted in Figure S2 (Supporting Information File 1), proves the presence of silicon in the ZnO/SiC_15 nanocomposite.

The formation of nanocomposites is accompanied by a significant increase in the electrical resistance of the material, in comparison with ZnO nanofibers, over the entire temperature range studied (Table 1). The resistance of SiC under these conditions is in the range of 10^9–10^{11} Ohm, which corresponds to the upper limit of the measurement range of the used setup. In the temperature range T = 400–550 °C, the conductivity of ZnO nanofibers and ZnO/SiC nanocomposites has an activation character (Figure 7). From the Arrhenius equation $\ln G = E_a/k_BT$, where G is the material conductance, k_B is the Boltzmann constant, the values of the activation energy E_a were calculated. For ZnO nanofibers, E_a = 0.40 ± 0.04 eV. This value lies within the error with the potential barrier at the grain boundaries eV_s (the surface potential barrier energy between particles of nanocrystalline zinc oxide) determined by the method of temperature-stimulated conductance measurements [29,30] as eV_s = 0.44 eV at T = 500 °C [31]. The creation of ZnO/SiC nanocomposites leads to an increase in the activation energy of conductivity up to 0.71–0.78 eV, and the value of E_a does not depend on the SiC content in nanocomposites (within the error, Table 1). The growth of the electrical resistance and E_a can be associated with an increase in the concentration of surface oxygen species (confirmed by XPS), which form different acceptor levels at the ZnO surface and at the ZnO/SiC heterojunction.

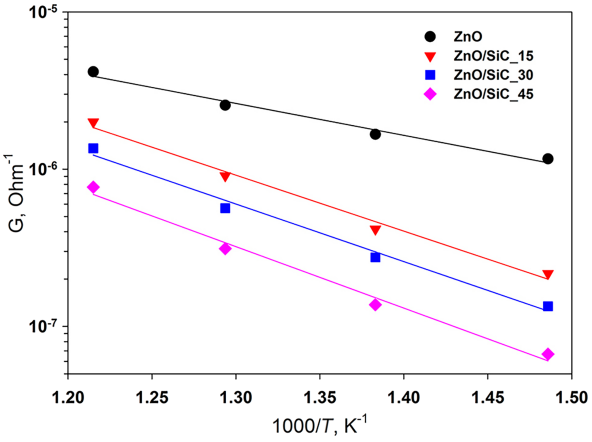

Figure 7: The conductance, G, of ZnO nanofibers and ZnO/SiC nanocomposites in the temperature range 400–550 °C.

The sensor properties of the synthesized materials were investigated by in situ conductivity measurements. Figure 8 shows the change in the resistance of ZnO nanofibers and ZnO/SiC nanocomposites with a periodic change in the composition of the gas phase in the presence of NH_3 (Figure 8a,b) and CO (Figure 8c,d) in dry air (Figure 8a,c) and at relative humidity RH_{25} = 30% (at 25 °C, Figure 8b,d). In all cases, in the presence of a reducing gas, CO or NH_3, a decrease in the material

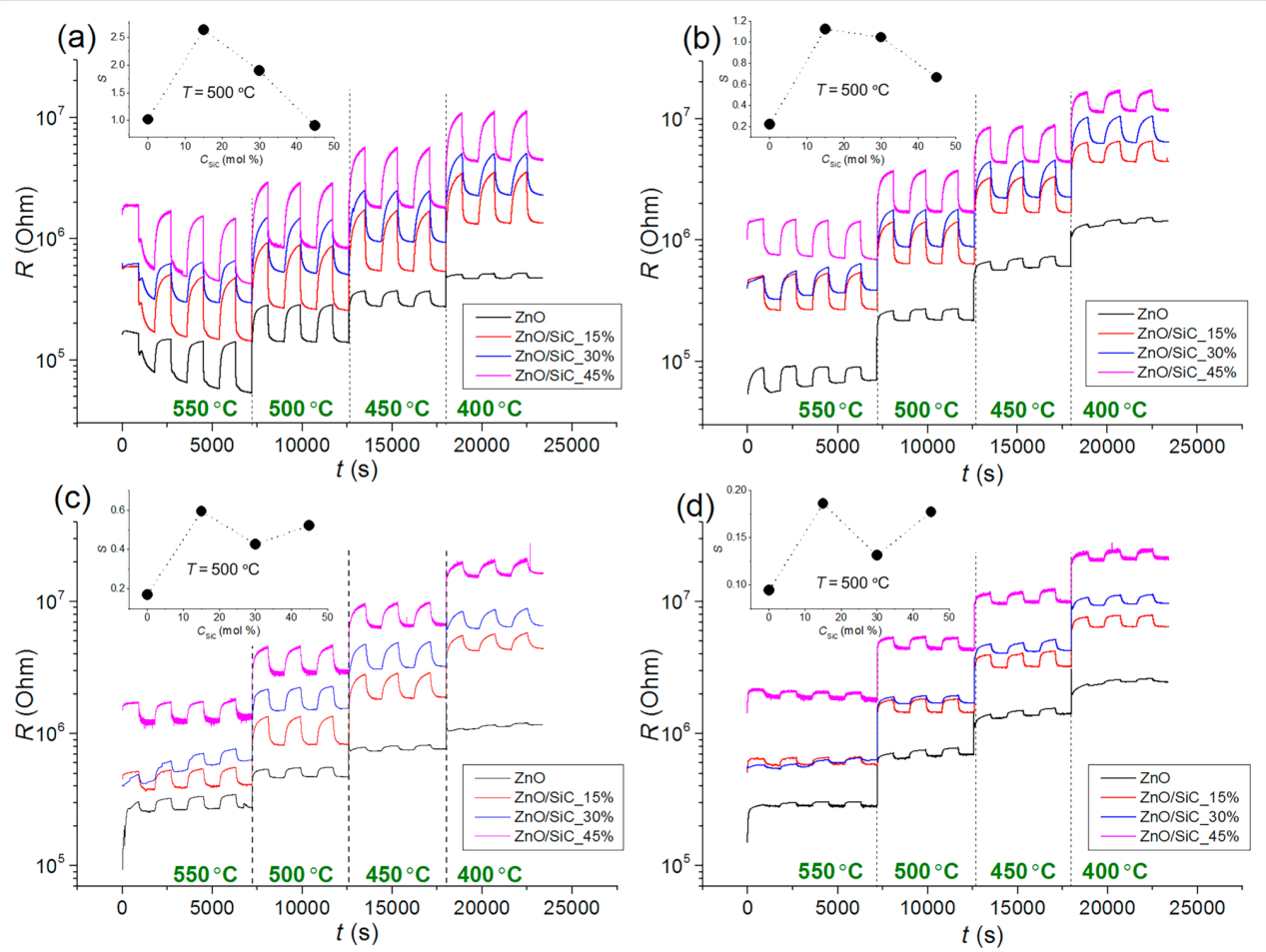

Figure 8: Change in the resistance of ZnO nanofibers and ZnO/SiC nanocomposites with a periodic change in the composition of the gas phase in the presence of 20 ppm NH_3 (a,b) and 20 ppm CO (c,d) in dry air (a,c) and at relative humidity RH_{25} = 30% (b,d). Insets: Sensor response dependence on SiC content in nanocomposites.

resistance is observed due to reaction of the target gases with the oxygen chemisorbed on the surface of n-type semiconductor materials:

$$\beta \cdot CO_{(gas)} + O^{-\alpha}_{\beta(ads)} \rightarrow \beta \cdot CO_{2(gas)} + \alpha \cdot e^{-} \quad (1)$$

$$2\beta \cdot NH_{3(gas)} + 3O^{-\alpha}_{\beta(ads)} \rightarrow \beta \cdot N_{2(gas)} + 3\beta \cdot H_2O_{(gas)} \quad (2)$$

where $CO_{(gas)}$, $NH_{3(gas)}$ are molecules of carbon monoxide and ammonia in the gas phase, $O^{-\alpha}_{\beta(ads)}$ is a particle of chemisorbed oxygen, e^{-} is an electron released into the conduction band; $CO_{2(gas)}$, $N_{2(gas)}$, $H_2O_{(gas)}$ are the molecules of the reaction products desorbed from the surface of the material to the gas phase.

The data obtained allowed us to calculate the value of the sensor response as

$$S = \frac{R_{air} - R_{gas}}{R_{air}}, \quad (3)$$

where R_{air} is the resistance of the material in background air, and R_{gas} is the resistance of the material in the presence of the target gas (CO or NH_3). The temperature dependence of the sensor response is shown in Figure 9. The maximum sensor response of ZnO nanofibers is observed at operating temperatures in the range of 500–550 °C, and in the case of ZnO/SiC nanocomposites, at T = 450–500 °C for both reducing gases. In both cases, the formation of ZnO/SiC nanocomposites leads to an increase in the sensor response compared to the bare ZnO nanofibers. The nanocomposites ZnO/SiC_15 and ZnO/SiC_30 demonstrate the highest values of the sensor response. A further increase in the SiC content leads to an increase in resistance and a decrease in the sensor response of the nanocomposites. Thus, from the point of view of the measured values of the sensor response and the base resistance in the temperature range of

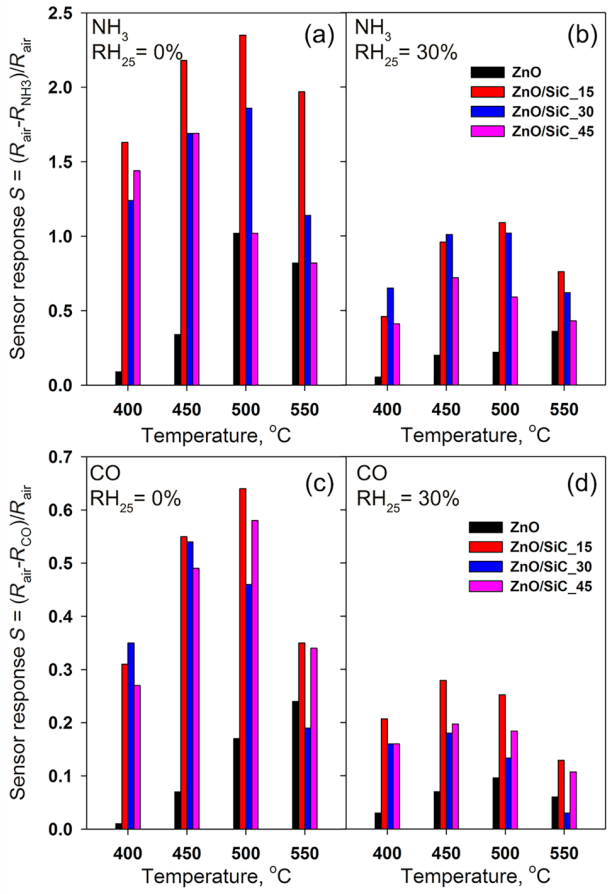

Figure 9: Temperature dependence of the sensor response of ZnO nanofibers and ZnO/SiC nanocomposites towards 20 ppm NH_3 (a,b) and 20 ppm CO (c,d) in dry air RH_{25} = 0% (a,c) and at relative humidity RH_{25} = 30% (b,d).

400–500 °C, the composition of the material, which corresponds to 15 mol % SiC, is optimal. An increase in air humidity up to RH_{25} = 30% leads to an approximately two-fold decrease in the sensor response to CO and NH_3.

The literature data characterizing conductometric gas sensors based on different MO/SiC systems are summarized in Table 2. It should be noted that there are few examples found in the literature [32-34], and all the found sources consider different gases. This does not allow for a correct comparison of the sensitivity of the materials obtained in this work with the analogues described in the literature.

The observed effect of SiC on the sensor response of ZnO nanofibers toward CO and NH_3 should be considered within the framework of a model involving the formation of n–n heterocontacts at the ZnO/SiC interface [35]. According to a previous report [36] the conduction band minimum (CBM) of n-type ZnO lies 0.4 eV lower than the CBM of n-type SiC. The calculated band alignment of the wurtzite (2H) ZnO and SiC phases is presented in previous reports [37,38]. Taking into account the difference in the band gap (E_g) of 2H-SiC (E_g = 3.3 eV [39]) and 3C-SiC (E_g = 2.36 eV [40]) polytypes, and assuming that the position of the valence band for these polytypes does not vary significantly, we constructed a diagram of the band alignment for ZnO and 3C-SiC phases (Figure 10). The estimated CBM position of wurtzite ZnO is 0.46 eV lower than that of 3C-SiC. The interface of an n–n junction transfers electrons into the lower energy conduction band [35]. The "accumulation layer" formed in this way can be depleted by subsequent oxygen adsorption on an enriched electron ZnO surface, increasing the potential energy barrier and enhancing the response

Table 2: Sensor response of conductometric gas sensors based on different MO/SiC sensitive materials.

Sensor material	Gas	Concentration, ppm	Temperature, °C	Relative humidity, %	Sensor response $\frac{R_{air}-R_{gas}}{R_{air}}$	Ref.
ZnO/SiC	CO	20	500	30	1.1	this work
	NH_3	20	450	30	0.27	
SnO_2/SiC	H_2	100	500	n/a	3.7	[32]
	xylene	100	500	n/a	0.8	
	acetone	100	500	n/a	1.8	
	isopropanol	100	500	n/a	1.6	
	methanol	100	500	n/a	2.1	
	ethanol	100	500	n/a	6.2	
SnO_2/SiC	NH_3	50	RT + UV[a]	30	0.2	[33]
	NO_2	5	RT + UV	30	0.12	
WO_3/SiC	H_2	20000	350	n/a	0.9	[34]

[a]At room temperature under UV light activation.

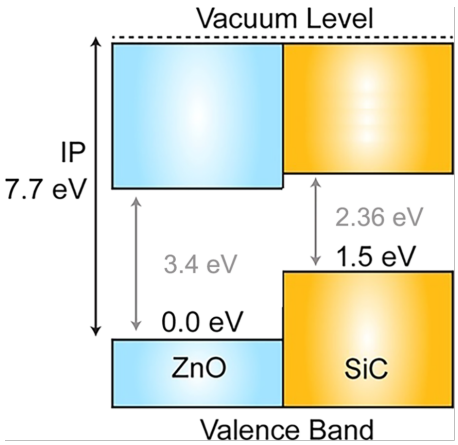

Figure 10: Estimated band alignment of the wurtzite ZnO and 3C-SiC phases. Adapted from [37] with permission from the American Chemical Society, copyright 2013.

formed due to reactions (Equation 1 and Equation 2). The decrease in the sensor response observed for all the samples with an increase in the concentration of water vapor in the gas phase may be due to the competition of oxygen and water molecules for the same adsorption centers on the ZnO surface [41].

Conclusion

ZnO/SiC nanocomposites based on ZnO nanofibers (wurtzite) and nanocrystalline SiC (3C polytype), obtained by the electrospining method, were investigated as sensitive materials for high-temperature resistive gas sensors. The introduction of SiC increased the sensitivity of ZnO nanofibers towards the reducing gases CO and NH_3 in the temperature range of 400–550 °C. This effect was accompanied by the increase in the activation energy of conductivity in this temperature range. The results obtained were interpreted in the context of the assumption of the formation of an n–n heterojunction at the ZnO/SiC interface, resulting in electron transfer from SiC to ZnO. The increase in the concentration of electrons in the near-surface layer of ZnO leads to an increase in the concentration of chemisorbed oxygen on its surface, which was confirmed by XPS. In turn, this determines an increase in the activation energy of conductivity and causes an increase in the sensor response of ZnO/SiC nanocomposites compared with ZnO nanofibers.

Experimental

Materials synthesis

Nanocrystalline silicon carbide, SiC, and zinc oxide, ZnO, were prepared separately by electrospinning of polymer solutions followed by heat treatment in order to remove the polymer and crystallize the semiconductor material. The annealing conditions for polymer decomposition were determined by thermal analysis.

Fabrication of nanocrystalline SiC

Polycarbosilane (PCS) was used as a precursor. In a typical procedure, 1 g of PCS was dissolved in 10 mL of chloroform. After the PCS completely dissolved, 1 g of polyvinylpyrrolidone (PVP, M = 1 300 000) was added. The mixture was actively stirred for 5 h at 40 °C. The polymer solution was loaded in a plastic syringe with a metal needle (G21) with an internal diameter of 510 µm. The electrospinning was carried out at the conditions of 3 mL/h solution feed rate, with 150 mm distance and 6 kV voltage between the needle and metal collector. The formed fibrous tissue was collected in an alundum Al_2O_3 crucible and annealed stepwise in an argon atmosphere at 220 °C (2 h, heating rate 1 K/min), 600 °C (2 h, heating rate 1 K/min), and finally at 1150 °C (6 h, heating rate 2 K/min). The obtained amorphous SiC was additionally annealed using the spark plasma sintering (SPS) method on a Spark plasma sintering system (LABOX-625) at a temperature of 1600 °C for 1 h under vacuum. As a result, 3C-SiC nanofibers with a cubic structure were obtained. The final annealing step was performed in air at 700 °C for 1 h to remove the rest of the carbon.

Fabrication of ZnO nanofibers

Zinc acetate ($Zn(CH_3COO)_2{\cdot}2H_2O$) was used as a precursor. In a typical procedure, 200 mg of zinc acetate was dissolved in 10 mL of mixed (1:1) solvent composed of 2-methoxyethanol and isopropanol. After complete dissolution of zinc acetate, 900 mg of PVP was added and the mixture was actively stirred for 5 h at 40 °C. The electrospinning of the polymer solution was carried out at the conditions of 1 mL/h solution feed rate, with 125 mm distance and 12 kV voltage between the needle and metal collector. The fibrous material was collected and heated at 550 °C (5 h, heating rate 1 K/min) in air in order to remove the polymer and crystallize the ZnO.

Fabrication of gas sensors

ZnO/SiC nanocomposites containing 0, 15, 30, 45 and 100 mol % SiC were prepared by mixing components in a single homogeneous paste using a solution of α-terpineol in ethanol as a binder. The sensors were fabricated by thick film technology via drop-deposition of the paste onto alumina micro-hotplates provided with vapor-deposited Pt contacts (0.3×0.2 mm^2) separated by a 0.2 mm gap and with embedded Pt-meanders. The paste was dried at room temperature in ambient air and then calcined at 250 °C in purified air for 20 h to remove the binder. The thick sensing layer was about 1×0.5 mm in size with the thickness of 5–7 µm. The list of the samples is given in Table 1.

Materials characterization

The phase composition was determined by X-ray diffraction (XRD) using a DRON-3 diffractometer (radiation Co Kα,

λ = 1.7903 Å). The crystallite size (d_{XRD}) of SiC and ZnO phases in nanofibers was estimated from the broadening of the (100) ZnO and (111) 3C-SiC XRD peaks using the Scherrer formula. The measurements of the specific surface area (S_{BET}) and analysis of the porosity of the samples were carried out by the method of low-temperature nitrogen adsorption on an ASAP 2010 instrument (Micromeritics). Prior to this, all samples were evacuated at a temperature of 300 °C to 4×10^{-1} Pa for 3 h. Based on the nitrogen adsorption isotherms obtained, the specific surface area, volume, and average pore size were calculated using BET (Brunauer–Emmett–Teller) and BJH (Barret–Johner–Halenda) models. The morphology of the nanofibers was studied by scanning electron microscopy (SEM) using a Carl Zeiss NVision 40 electron microscope with an intra-lens detector at an accelerating voltage of 5 kV. The IR spectra (FTIR) of the ZnO/SiC nanocomposites were taken on a Spectrum One (Perkin Elmer) spectrometer in transmission mode within the range 400–4000 cm^{-1} with 1 cm^{-1} steps. The XPS experiments were performed using an Axis Ultra DLD (Kratos) X-ray photoelectron spectrometer, equipped with a monochromatic Al Kα source. XPS spectra of core levels were fitted by Gaussian/Lorentzian convolution functions with simultaneous optimization of the background parameters. The background was simulated using a combination of a Shirley and a Tougaard background. The binding energies (BE) were corrected for the charge shift using the C 1s peak of graphitic carbon (BE = 284.8 eV) as a reference.

Gas sensor tests were performed by in situ conductivity measurements in an automatic set up with a flow chamber. The sensor resistance was measured at 1.3 V DC-voltage in situ under a controlled gas flow of 100 ± 0.1 mL/min at a temperature fixed in the range of 400–550 °C. Purified air with a pre-assigned humidity (RH = 0% and RH = 30% at 25 °C) was used as a background gas. The test gases containing CO (20 ppm) and NH_3 (20 ppm) were created from certified gas mixtures by the dilution with purified air with a pre-assigned humidity The corresponding gas flows were controlled by electronic mass-flow controllers (Bronkhorst).

Supporting Information

Survey X-ray photoelectron spectra of SiC, ZnO, ZnO/SiC_15 nanocomposite, and X-ray photoelectron spectra of ZnO/SiC_15 nanocomposite in the Si 2p region.

Supporting Information File 1

XPS data.
[https://www.beilstein-journals.org/bjnano/content/supplementary/2190-4286-10-151-S1.pdf]

Acknowledgements

The work was financially supported by RFBR grant No. 18-03-00091 and in part by a grant from the St. Petersburg State University – Event 3-2018 (id: 26520408). The authors are grateful to the Center of Collective Use of ISSP RAS, Dr. Svetlana Protasova and Dr. Andrei Ionov for assistance with the XPS measurements. The spectral research was carried out using the equipment purchased by funds of the Lomonosov Moscow State University Program of the Development. The SEM and EDX research was performed using the equipment of the Joint Research Center for Physical Methods of Research of Kurnakov Institute of General and Inorganic Chemistry of the Russian Academy of Sciences.

ORCID® iDs

Marina N. Rumyantseva - https://orcid.org/0000-0002-3354-0885
Alexander S. Frolov - https://orcid.org/0000-0001-7955-6359

References

1. Araújo, K.; Mahajan, D.; Kerr, R.; Silva, M. d. *Agriculture (Basel, Switz.)* **2017,** *7,* 32. doi:10.3390/agriculture7040032
2. Prasad, S.; Dhanya, M. S. Air Quality and Biofuels. In *Environmental Impact of Biofuels;* Dos Santos Bernardes, M. A., Ed.; InTech: Rijeka, Croatia, 2011; pp 227–250. doi:10.5772/17889
3. Liu, Y.; Parisi, J.; Sun, X.; Lei, Y. *J. Mater. Chem. A* **2014,** *2,* 9919–9943. doi:10.1039/c3ta15008a
4. Richter, D.; Fritze, H. High-Temperature Gas Sensors. In *Gas Sensing Fundamental;* Kohl, D.; Wagner, T., Eds.; Springer: Berlin, Germany, 2013; pp 1–46. doi:10.1007/5346_2013_56
5. Moos, R.; Sahner, K.; Fleischer, M.; Guth, U.; Barsan, N.; Weimar, U. *Sensors* **2009,** *9,* 4323–4365. doi:10.3390/s90604323
6. Gerhardt, R., Ed. *Properties and Applications of Silicon Carbide;* InTech: Rijeka, Croatia, 2011. doi:10.5772/615
7. Andersson, M.; Lloyd Spetz, A.; Pearce, R. Recent trends in silicon carbide (SiC) and graphene based gas sensors. In *Semiconductor gas sensors;* Jaaniso, R.; Kiang, O., Eds.; Woodhead Publishing Series in Electronic and Optical Materials; Woodhead Publishing Ltd.: Oxford, United Kingdom, 2013; pp 117–158. doi:10.1533/9780857098665.2.117
8. Pavelko, R. G.; Vasiliev, A. A.; Vilanova, X.; Sevastyanov, V. G. Synthesis of sensing composite SnO_2-SiC using one dimensional SiC nanostructures. In *Proceedings of PhD Students Work Shop on Nanoelectronic and Photonics Systems,* Spain, Tarragona; 2006; pp 51–52.
9. Schalwig, J.; Kreisl, P.; Ahlers, S.; Muller, G. *IEEE Sens. J.* **2002,** *2,* 394–402. doi:10.1109/jsen.2002.806214
10. Hunter, G. W.; Neudeck, P. G.; Knight, D.; Liu, C. C.; Wu, Q. H.; Chen, L. Y. Reactive-insulator SiC-based Schottky Diodes as Gas Sensors. Tech Briefs: Physical Sciences, 1999; http://www.nasatech.com/Briefs/Jan99/LEW16544.html (accessed Feb 26, 2019).
11. Trinchi, A.; Wlodarski, W.; Li, Y. X.; Faglia, G.; Sberveglieri, G. *J. Phys. D: Appl. Phys.* **2005,** *38,* 754–763. doi:10.1088/0022-3727/38/5/014

12. Casaals, O.; Becker, T.; Godignon, P.; Romano-Rodrigues, A. SiC-based MIS gas sensor for CO detection in very high water vapor environment. The 14th International Meeting on Chemical Sensors, Nuremberg, Germany, May 20–23, 2012; .
13. Lloyd Spetz, A.; Unéus, L.; Svenningstorp, H.; Tobias, P.; Ekedahl, L. G.; Larsson, O.; Göras, A.; Savage, S.; Harris, C.; Mårtensson, P.; Wigren, R.; Salomonsson, P.; Häggendahl, B.; Ljung, P.; Mattsson, M.; Lundström, I. *Phys. Status Solidi A* **2001,** *185,* 15–25. doi:10.1002/1521-396x(200105)185:1<15::aid-pssa15>3.0.co;2-7
14. Schalwig, J.; Kreisl, P.; Ahlers, S.; Muller, G. *IEEE Sens. J.* **2002,** *2,* 394–402. doi:10.1109/jsen.2002.806214
15. Fawcett, T. J.; Reyes, M.; Lloyd Spetz, A.; Saddow, S. E.; Wolan, J. T. *MRS Online Proc. Libr.* **2006,** *911,* 0911-B12-06. doi:10.1557/proc-0911-b12-06
16. Li, Z.; Wang, C. *One-Dimensional nanostructures. Electrospinning technique and unique nanofibers;* Springer: Berlin, Germany, 2013. doi:10.1007/978-3-642-36427-3
17. Mondal, K.; Sharma, A. *RSC Adv.* **2016,** *6,* 94595–94616. doi:10.1039/c6ra21477k
18. Liu, H. A.; Balkus, K. J., Jr. *Mater. Lett.* **2009,** *63,* 2361–2364. doi:10.1016/j.matlet.2009.08.009
19. Wang, B.; Sun, L.; Wu, N.; Wang, Y. *Ceram. Int.* **2017,** *43,* 10619–10623. doi:10.1016/j.ceramint.2017.05.068
20. Thomas, D. G. *J. Phys. Chem. Solids* **1959,** *10,* 47–51. doi:10.1016/0022-3697(59)90124-6
21. Davydov, A. A. *Molecular spectroscopy of oxide catalyst surfaces;* John Wiley & Sons, Ltd.: Chichester, United Kingdom, 2003. doi:10.1002/0470867981
22. Nakamoto, K. *Infrared and Raman Spectra of Inorganic and Coordination Compounds,* 6th ed.; John Wiley & Sons, Inc.: Hoboken, NJ, U.S.A., 2008. doi:10.1002/9780470405840
23. Niu, Y.; Zhang, X.; Zhao, J.; Tian, Y.; Li, Y.; Yan, X. *RSC Adv.* **2014,** *4,* 28456. doi:10.1039/c4ra02769h
24. Önneby, C.; Pantano, C. G. *J. Vac. Sci. Technol., A* **1997,** *15,* 1597–1602. doi:10.1116/1.580951
25. Leontiev, S. A.; Koshcheev, S. V.; Devyatov, V. G.; Cherkashin, A. E.; Mikheeva, é. P. *J. Struct. Chem.* **1997,** *38,* 725–731. doi:10.1007/bf02763884
26. Kotsis, K.; Staemmler, V. *Phys. Chem. Chem. Phys.* **2006,** *8,* 1490–1498. doi:10.1039/b515699h
27. Liangyuan, C.; Zhiyong, L.; Shouli, B.; Kewei, Z.; Dianqing, L.; Aifan, C.; Liu, C. C. *Sens. Actuators, B* **2010,** *143,* 620–628. doi:10.1016/j.snb.2009.10.009
28. Chen, M.; Wang, X.; Yu, Y. H.; Pei, Z. L.; Bai, X. D.; Sun, C.; Huang, R. F.; Wen, L. S. *Appl. Surf. Sci.* **2000,** *158,* 134–140. doi:10.1016/s0169-4332(99)00601-7
29. Clifford, P. K.; Tuma, D. T. *Sens. Actuators* **1982,** *3,* 255–281. doi:10.1016/0250-6874(82)80027-9
30. Lantto, V.; Rompplainen, P.; Leppävuori, S. *Sens. Actuators* **1988,** *14,* 149–163. doi:10.1016/0250-6874(88)80062-3
31. Vorobyeva, N. A.; Rumyantseva, M. N.; Forsh, P. A.; Gaskov, A. M. *Semiconductors* **2013,** *47,* 650–654. doi:10.1134/s1063782613050242
32. Wang, B.; Wang, Y.; Lei, Y.; Xie, S.; Wu, N.; Gou, Y.; Han, C.; Shi, Q.; Fang, D. *J. Mater. Chem. C* **2016,** *4,* 295–304. doi:10.1039/c5tc02792f
33. Karakuscu, A.; Ponzoni, A.; Comini, E.; Sberveglieri, G.; Vakifahmetoglu, C. *Int. J. Appl. Ceram. Technol.* **2014,** *11,* 851–857. doi:10.1111/ijac.12295
34. Fominski, V. Y.; Grigoriev, S. N.; Demin, M. V.; Zuev, V. V.; Romanov, R. I.; Volosova, M. A. *J. Surf. Invest.: X-Ray, Synchrotron Neutron Tech.* **2016,** *10,* 652–657. doi:10.1134/s1027451016030204
35. Miller, D. R.; Akbar, S. A.; Morris, P. A. *Sens. Actuators, B* **2014,** *204,* 250–272. doi:10.1016/j.snb.2014.07.074
36. Zhang, Y.; Lin, N.; Li, Y.; Wang, X.; Wang, H.; Kang, J.; Wilks, R.; Bär, M.; Mu, R. *Sci. Rep.* **2016,** *6,* 23106. doi:10.1038/srep23106
37. Walsh, A.; Buckeridge, J.; Catlow, C. R. A.; Jackson, A. J.; Keal, T. W.; Miskufova, M.; Sherwood, P.; Shevlin, S. A.; Watkins, M. B.; Woodley, S. M.; Sokol, A. A. *Chem. Mater.* **2013,** *25,* 2924–2926. doi:10.1021/cm402237s
38. Farrow, M. R.; Buckeridge, J.; Lazauskas, T.; Mora-Fonz, D.; Scanlon, D. O.; Catlow, C. R. A.; Woodley, S. M.; Sokol, A. A. *Phys. Status Solidi A* **2017,** *214,* 1600440. doi:10.1002/pssa.201600440
39. Patrick, L.; Hamilton, D. R.; Choyke, W. J. *Phys. Rev.* **1966,** *143,* 526–536. doi:10.1103/physrev.143.526
40. Goldberg, Y.; Levinshtein, M. E.; Rumyantsev, S. L. Silicon carbide (SiC). In *Properties of Advanced Semiconductor Materials GaN, AlN, SiC, BN, SiC, SiGe;* Levinshtein, M. E.; Rumyantsev, S. L.; Shur, M. S., Eds.; John Wiley & Sons, Inc.: New York, NY, U.S.A., 2001; pp 93–148.
41. Barsan, N.; Weimar, U. *J. Electroceram.* **2001,** *7,* 143–167. doi:10.1023/a:1014405811371

License and Terms